ESA CONTRACT REPORT

Contract Report to the European Space Agency

Forward operator developments - Errors and biases in representativity

September 2009

Authors: S. Di Michele, O. Stiller and R. Forbes

WP-1000 report for ESA contract 1-5576/07/NL/CB:
Project QuARL - Quantitative Assessment of the Operational Value of Space-Borne Radar and Lidar Measurements of Cloud and Aerosol Profiles

European Centre for Medium-Range Weather Forecasts
Europäisches Zentrum für mittelfristige Wettervorhersage
Centre européen pour les prévisions météorologiques à moyen terme

ECMWF

Series: ECMWF - ESA Contract Report

A full list of ECMWF Publications can be found on our web site under:
http://www.ecmwf.int/publications/

Contact: library@ecmwf.int

European Centre for Medium-Range Weather Forecasts
Shinfield Park, Reading, RG2 9AX, England

Contract Report to the European Space Agency

Forward operator developments - Errors and biases in representativity

Authors: S. Di Michele, O. Stiller and R. Forbes

WP-1000 report for ESA contract 1-5576/07/NL/CB:
Project QuARL - Quantitative Assessment of the Operational Value of Space-Borne Radar and Lidar Measurements of Cloud and Aerosol Profiles

European Centre for Medium-Range Weather Forecasts
Shinfield Park, Reading, Berkshire, UK

September 2009

ABSTRACT

A radar-and-lidar reflectivity forward model is required to enable the verification and data assimilation work planned for this project using CloudSat and CALIPSO data. At ECMWF, a radar forward operator exists, explicitily designed for assimilation purposes. It has been used for ground-based 14 and 35 GHz radar observations and it has been adapted for the CloudSat radar frequency of 94 GHz in this study. Also, a recent pre-existing radar-and-lidar forward operator, called CFMIP (Cloud Feedback Model Intercomparison Project) Observation Simulator Package (COSP), has been implemented. This operator is being used only for verification purposes since the assimilation system requires stringent specifications of computationally efficiency. The first part of this report compares the two forward models, shows their sensitivities to different microphysical and sub-grid variability assumptions and describes the changes to the ECMWF forward model for use in this project. Since CloudSat and CALIPSO observations have high vertical and horizontal resolution, but they lack of spatial coverage, it is important to address the issue of representativity errors. These errors are likely to form a large part of the total observation error and their magnitude varies for different wheather regimes. The second part of this report presents a statistical approach for computing a flow dependent estimate for the representativity error. The proposed method derives a quasi-empirical relationship between the error and a statistical measure (”score”) which can be computed from satellite measurements. The robustness of this method is demonstrated for observations which have larger horizontal coverages and therefore allow a direct verification.

Contents

1 Introduction

For Numerical Weather Prediction (NWP) systems, verification, monitoring and data assimilation require a forward operator to generate the model equivalent to the observations. Its definition affects biases, observation and modelling errors and assimilation performance.

In the first part of the first work package (WP-1000) of the QuARL project, existing forward operators for radar and lidar have been adapted for use in the verification and data assimilation work later in the project. The CFMIP (Cloud Feedback Model Intercomparison Project) Observation Simulator Package (COSP) which contains a radar simulator for CloudSat (Haynes *et al.*, 2007) and a lidar simulator for CALIPSO (Chiriaco *et al.*, 2006) has been implemented at ECMWF and used for model verification. Since the assimilation system requires computationally efficient operators, an ECMWF radar reflectivity model used in the past for assimilation studies of ground-based 14 and 35 GHz radar observations (Benedetti and Janisková 2004, Janisková 2004, Lopez *et al.* 2006) has been adapted for the CloudSat radar frequency of 94 GHz. Section 2 compares these radar reflectivity forward models, describes their sensitivities to different microphysical and sub-grid variability assumptions and recommends the appropriate forward model for use in this project.

While the capability of a forward operators to mimic the evolution of radar or lidar rays faithfully is important, this does not guarantee an accurate comparison between model output and CloudSat or CALIPSO observations. One error source which, indeed, is intrinsic to most model-observation comparisons stems from the fact that measurements are generally valid on different space and time scales from those which are represented by the model variables. For CloudSat and CALIPSO observations the corresponding representativity (or representativeness) error is potentially very large as their horizontal coverage is very small compared to that of a NWP model gridbox. For this reason great effort has been made to estimate this error. As, from the beginning of the project it was recognized that the size of the representativity error is strongly dependent on weather regime, a flow dependent error measure has been developed. Errors and biases related to the representativity problem are discussed in Section 3.

2 Forward operator: adaptation and development

The A-Train is a constellation of five satellites flying in formation. This constitutes a unique opportunity to provide, in a synergistic way, a multitude of measurements about aerosol, atmospheric water (in all phases), ozone and trace gases. Among the instruments, both CloudSat radar and CALIPSO lidar have a fundamental role in improving the understanding of the physics of clouds, through the information about the vertical structure. CloudSat carries the Cloud Profiling Radar (CPR), a 94-GHz nadir-looking radar that measures the power backscattered by clouds with a sensitivity threshold of -26 dBZ.

At ECMWF, a procedure has been implemented for the assimilation of radar observations (Lopez *et al.*, 2006). In this context, a forward operator for reflectivities (ZmVar) was designed to meet the requirements of the assimilation system, i.e., to allow the coding of its adjoint counterpart, to be computationally efficient, and to have a certain degree of flexibility (e.g., for the definition of the optical properties). The focus of this study is on the adaptation of ZmVar to simulate CloudSat radar observations. For this purpose, ZmVar will be compared with a recent forward operator developed by the Cloud Feedback Model Intercomparison Project (CFMIP) community which is called the CFMIP Observation Simulator Package (COSP). Both ZmVar and COSP are designed to simulate the signal (i.e. reflectivities) which CloudSat and CALIPSO would measure if they were confronted with the atmospheric conditions obtained from a global circulation model.

For validation, the simulated CloudSat radar reflectivities from ZmVar will be compared to the corresponding real observations. For this the ZmVar input profiles (which are extracted from the ECMWF integrated forecast model IFS) have to be geographically and temporally coincident with CloudSat observations.

2.1 Reflectivity models

2.1.1 ZmVar

ZmVar was first developed at ECMWF for the Precipitation Radar on board the Tropical Rainfall Measuring Mission satellite (Benedetti *et al.*, 2005). First, for each hydrometeor, h, the backscattering cross section, $\sigma^h_{bs}(D)$, and the extinction cross section, $\sigma^h_{ext}(D)$, are computed for a single particle (of size D) using the Mie solution for a sphere (at the specified temperature and the given wavelength, λ). The assumption of sphericity for ice particles is an approximation that avoids the use of a more complex and computationally expensive solution to the problem (e.g. Discrete Dipole Approximation). This assumption, although rather simple, is reasonable since the corresponding errors are smaller than those resulting from the imperfect knowledge of the ice particles' size spectrum.

To deduce the optical properties of water or ice particles one needs a model for the interaction with the radiative electro-magnetic field. The key quantity of such a description is the permittivity $\varepsilon = \varepsilon^{'} + i\varepsilon^{''}$ which describes the impact that the internal distribution of charges has on an external dielectric field. Generally, the response of the internal charges to an external field is time dependent and also a function of temperature. As a result, the permittivity depends on the frequency of the external field as well as the temperature of the responding medium. The real part $\varepsilon^{'}$ of ε describes the dispersion of the phase delay induced on an electromagnetic wave passing through a medium, while $\varepsilon^{''}$ represents the loss of energy. The complex refractive index $m = m^{'} - i\, m^{''}$ is related to ε through $m = \sqrt{\varepsilon}$. ZmVar uses the water permittivity model of Liebe *et al.* (1991), while for ice the model of Mätzler and Wegmüller (1988) is implemented. Frozen hydrometeors are modelled as particles composed of an air-ice mixture, i.e. with a density ρ lower than the one of pure ice. The corresponding effective permittivity is evaluated using the model of Maxwell Garnett (1904). It is also worth mentioning that ZmVar includes a model for treating melting ice particles below the freezing level (Bauer *et al.*, 2000). However, the modelling of the melting layer is of secondary importance here, since the bright band phenomenon is weak at a frequency of 94 GHz due to attenuation (Kollias and Albrecht, 2005). In addition, the melting layer is resolved only very crudely by the coarse vertical resolution of the model.

Simulating radar reflectivity requires not only the knowledge of the single particle scattering/extinction properties, but also the number distribution for particles of a given size D (into which the hydrometeor content w is divided) has to be known for each hydrometeor type h. For this a particle size distribution (PSD) $N^h(D)$ is generally assumed from which the equivalent radar reflectivity Z^h can be evaluated by integrating over the size spectrum:

$$Z^h = \frac{\lambda^4}{\pi^5 |K_w|^2} \int_{D^h_{min}}^{D^h_{max}} \sigma^h_{\mathrm{bs}}(D) N^h(D) dD \tag{2.1}$$

where D^h_{min} and D^h_{max} are pre-defined values of limits for the particle size and K_w is defined as:

$$K_w = \frac{m_w^2 - 1}{m_w^2 + 2}. \tag{2.2}$$

Here m_w is the water refractive index and depends on the radar frequency as well as the reference temperature. A formula similar to Eq. (2.1) can be written to evaluate the volumetric extinction β^h:

$$\beta^h = \int_{D^h_{min}}^{D^h_{max}} \sigma^h_{ext}(D) N^h(D) dD. \tag{2.3}$$

For computational efficiency, ZmVar uses a pre-calculated table of hydrometeor optical properties (extinction and backscattering coefficients). This look-up table contains volumetric extinction and equivalent reflectivity of predefined hydrometeor types specified on a range of temperatures and hydrometeor contents (HCs), for the relevant frequency (i.e. 94 GHz in our case). The following discretization is used:

- 70 values of temperatures, [234-303] K for liquid particles and [204-273] K for frozen particles.
- 401 values of hydrometeor content, logarithmically scaled in the range [0.0001-1] g/m^3.

ZmVar has the capability to model six hydrometeor types: rain, snow, graupel, hail, cloud liquid water, and cloud ice water. Since the ECMWF model does not directly represent the graupel and hail categories associated with deep convection, only non precipitating (cloud ice) and precipitating (snow) frozen hydrometeors are considered in this study.

Cloud liquid and cloud ice are assumed to follow a Modified-Gamma distribution, also called the *Khrgian Mazin distribution* (Deirmendjian, 1969). It prescribes the number of particles per radius r according to the following expression:

$$n(r) = \mathrm{a} r^{\alpha} e^{-\mathrm{b} r^{\gamma}} \tag{2.4}$$

Constants a, b and γ are real and positive, while α is a positive integer.

PSDs of other hydrometeors are modelled as a Gamma distribution (and the exponential distribution is a special case when $\mu = 0$):

$$N(D) = N_0 D^{\mu} e^{-\frac{D}{D_n}} \tag{2.5}$$

where N_0 is the number concentration intercept parameter (units: m^{-4}), μ is the shape parameter and D_n is the characteristic diameter.

Each of these distributions has two, three or four degrees of freedom. To fully define the number of particles per size bin, additional assumptions have to be made which specify all but one degree of freedom. This last degree of freedom is then determined from the HC (mass) conservation. PSDs and values of their fixed parameters for each hydrometeor type as set within ZmVar are given in Tab. 2.1.1 (second and third column).

To simulate radar measurements at 94 GHz, it is important to properly model the density ρ of frozen particles. ZmVar assigns a different density to each ice category. The value doesn't depend on the particle size. The forth column of Tab. 2.1.1 contains the default values of particle density originally specified in ZmVar.

Hydrometeor	**Distribution type**	**Distribution parameters**	**Density** $[g/cm^3]$
Cloud Liquid	Mod. Gamma	$\alpha = 2$ $b = 0.425$ $\gamma = 1.0$	1.0
Cloud Ice (Pristine)	Mod. Gamma	as above	0.916
Rain	Gamma	$\mu = 2$ $N_0 = 0.08\,cm^{-4}$	1.0
Snow	Exponential	$N_0 = 0.03\,cm^{-4}$	0.1
Graupel	Gamma	$\mu = 0$ $N_0 = 0.04\,cm^{-4}$	0.4
Hail	Gamma	$\mu = 0$ $N_0 = 0.04\,cm^{-4}$	0.916

Table 2.1.1*: Original parametrization of hydrometeor particle properties in ZmVar.*

The way reflectivity is computed by ZmVar is schematically given in Fig. 2.1. First, the look-up table is read and stored into memory. Values of reflectivity due to each single hydrometeor type are then evaluated by means of a bilinear interpolation on the values of temperature and HC of the input profile. Equivalent reflectivity of all hydrometeors are then combined:

$$Z = \sum_{h=1,N_{HYD}} Z^h \tag{2.6}$$

Simulated measurements are finally obtained taking into account the attenuation of the signal along the path:

$$Z^a = Z\,e^{-2\tau} \tag{2.7}$$

where τ is the optical depth between the layer considered and the top of the atmosphere. The power emitted and returned to the radar is attenuated by clouds above, but also by atmospheric gases. This effect is not negligible at 94 GHz, but it was not included in the original version of ZmVar. In the context of this project, the attenuation due to gases has been considered when evaluating the attenuated reflectivity (together to the one due to the hydrometeors) using the model of Liebe *et al.* (1992). The impact on the resulting Z has been investigated using ZmVar to simulate 94 GHz reflectivities corresponding to a set of 50 ECMWF model profiles simulated with and without considering gas attenuation. Fig. 2.2 compares results of two runs for three model levels (higher model levels correspond to heights closer to surface). We can note differences from 2 to 5 dBZ, depending on the bin height.

2.1.2 COSP

The simulator of radar observations within COSP is the QuickBeam reflectivity simulator. QuickBeam has been developed at Colorado State University in the framework of the CloudSat mission. An overview of this software is given in Haynes *et al.* (2007), while an example of application can be found in Bodas-Salcedo *et al.* (2008). Given a list of input variables relative to a cloud profile (namely: pressure, temperature, humidity, and mixing ratio of hydrometeors), QuickBeam evaluates the corresponding values of equivalent radar reflectivity at a specified radar frequency. The number and the type of hydrometeors (in liquid and solid phases) depends on what is available from the cloud/climate model and can be specified by the user.

The way QuickBeam evaluates reflectivities closely resembles ZmVar. Hydrometeors are assumed as a collection of spherical particles and therefore backscattering is evaluated using Mie theory. In QuickBeam

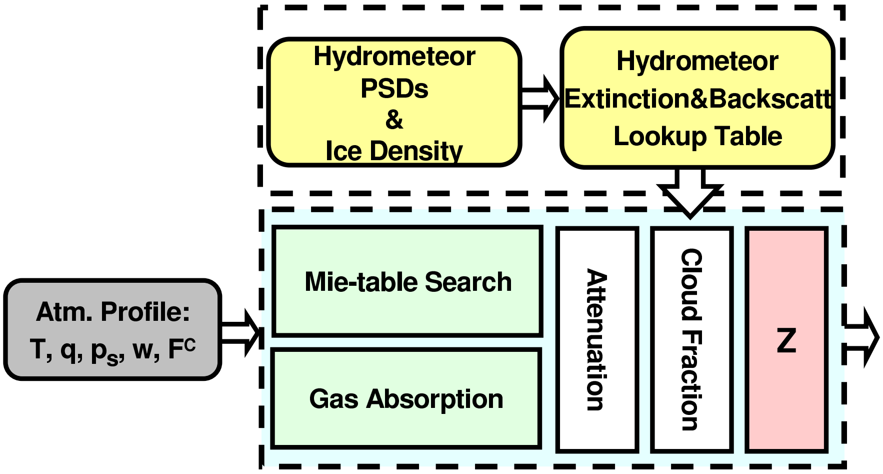

Figure 2.1: Schematic representation of ZmVar.

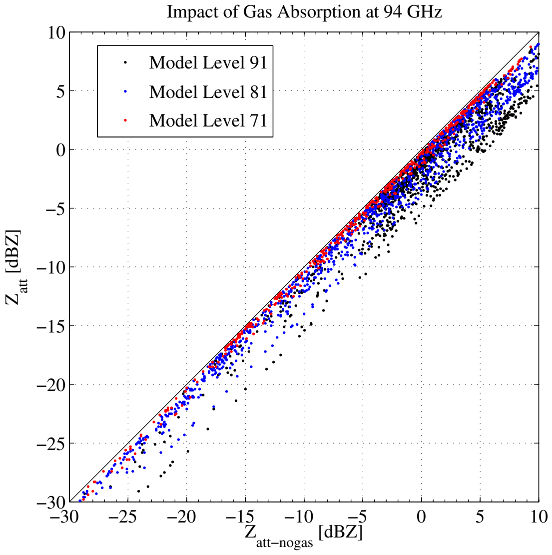

Figure 2.2: Comparison of 94 GHz ZmVar reflectivities simulated with and without inclusion of atmospheric gas absorption at model levels 91 (level closest to the surface), 81, and 71 corresponding approximately to 1010 hPa, 925 hPa and 700 hPa, respectively.

water permittivity is evaluated according to the model of Ray (1972), while the model of Warren (1984) is used for ice permittivity. QuickBeam allows the user to represent a number of different forms of hydrometeor PSDs. The following PSDs are modelled:

- Gamma:

$$N(D) \quad = \quad N_t \frac{1}{\Gamma(\mu) D_n} \left(\frac{D}{D_n}\right)^{\mu-1} D^{\mu} e^{-\frac{D}{D_n}} \tag{2.8}$$

where N_t, D_n (the characteristic diameter) and μ (the shape parameter) are real and positive. Note that the mean diameter $\overline{D}$ is related to D_n and μ through the following expression:

$$\overline{D} = \frac{\Gamma(\mu+1)}{\Gamma(\mu)} D_n \tag{2.9}$$

- Exponential:

$$N(D) = N_0 e^{-\frac{D}{D_n}} \tag{2.10}$$

where N_0 and D_n are real and positive.

- Power law:

$$N(D) = \mathrm{A} D^b \tag{2.11}$$

where A and b are real and positive.

- Log normal:

$$n(r) = \frac{N_t}{\sqrt{2\pi}(\ln\sigma_g) r} e^{-\frac{\ln^2(r/r_g)}{2(\ln\sigma_g)^2}} \tag{2.12}$$

where r_g is the geometric mean particle radius, N_t is the total particle number concentration, and σ_g is the geometric standard deviation.

- Mono dispersed:

$$N(D_0) = N_0 \tag{2.13}$$

Note that QuickBeam also allows specifying as input, beside the liquid/ice water contents, the particle effective radius. This option is useful when working with profiles generated from models, many of which are able to diagnose the effective radius of (non-precipitating) particles, varying along the profile.

As mentioned above, hydrometeor PSDs are input parameter to QuickBeam. The choices made in the implementation of QuickBeam within COSP are summarized in the second and third columns of Table 2.1.2. PSDs of precipitating hydrometeors (rain and snow) are modelled as exponential, a reasonable approximation of observed rain and snow size distributions. The fixed size parameter is the intercept N_0, representing the fact (characteristic in precipitation) that the number of particles with larger size tends to increase as water content increases. For cloud liquid a lognormal distribution is used. This function has been chosen because it represents the drop size spectra for cloud droplets observed from *in situ* measurements. The cloud ice size distribution is modelled as Gamma, which has a spread wider than the lognormal. As the water content increases, differently from the exponential, the shape of the Gamma and lognormal PSDs is unchanged.

Differently from ZmVar, in QuickBeam particle density can also be treated expressing the particle mass as a power law function of its diameter:

$$m(D) = \alpha D^\beta \tag{2.14}$$

In case of frozen particles, it has to be interpreted as a ‘mean diameter’, i.e. an average dimension of the particle. Table 2.1.2 (forth column) contains the values of the coefficients used in COSP. Note that they are valid when density is expressed in kgm^{-3} and the diameter in μm. Their values will be discussed in Section 2.1.4. Differently from ZmVar, QuickBeam doesn’t contain a specific model for melting ice particles. The gas absorption model used in QuickBeam, which takes into account the local power absorption from oxygen and water vapour, is also (slightly) different from ZmVar: the one of Liebe (1985) is used.

Hydrometeor	***Distribution Type***	***Distribution parameters***	***Density parameters***
Cloud Liquid	Lognormal	$ln\,\sigma_g = 0.3$ $r_g = 6\,\mu m$	$\alpha = 524$ $\beta = 3$
Cloud Ice	Gamma	$\overline{D} = 40\,\mu m$ $\mu = 2$	$\alpha = 110.8$ $\beta = 2.91$
Rain	Exponential	$N_0 = 0.08\,cm^{-4}$	$\alpha = 524$ $\beta = 3$
Snow	Exponential	$N_0 = 0.03\,cm^{-4}$	$\rho = 0.1\,g\,cm^{-3}$

Table 2.1.2: *Parametrization of hydrometeor particle properties in COSP.*

2.1.3 Differences in simulated reflectivity

In this section, ZmVar and COSP are compared simulating 94 GHz reflectivities (Zs) separately for each hydrometeor (for a given temperature, without taking into account gas and hydrometeor attenuation). Reflectivities are generated for a range of hydrometeor contents. This allows quantifying how different modelling assumptions (made for each category) impact simulated reflectivities.

(a) Rain

In their original configurations, ZmVar and COSP make different assumptions for the rain PSD: the first uses a Gamma distribution, while the second uses the Marshall Palmer distribution (Fig. 2.3). Corresponding simulated reflectivities are given in Fig. 2.4. ZmVar produces higher reflectivities across the range of water contents. The reason can be identified by the fact that the Gamma distribution puts more particles in the range of sizes where the single particle backscattering is highest, i.e. between 0.05 and 0.15 cm (Fig. 2.5). Fig 2.5 also highlights the different discretization of the diameters used for the Mie calculations by COSP and ZmVar: logarithmic for COSP and linear for ZmVar. Although the linear discretization is preferable, because it avoids possible aliasing effects for the larger drop sizes, the impact on final reflectivity values is found to be negligible for rain. In fact, when a Marshall Palmer exponential PSD is assumed in both ZmVar and COSP, the reflectivities are effectively the same.

(b) Cloud Liquid

As mentioned in the previous section, cloud liquid is assumed to follow a lognormal distribution in COSP. In ZmVar instead, a Modified Gamma distribution is used, as proposed by Deirmendjian (1969). The two PSDs are shown in Fig. 2.6. The main differences occur for diameters up to 0.01 cm, where the Modified Gamma puts more particles. In particular, we observe that, below 0.005 cm the Modified Gamma is higher by several orders of magnitude. Consequently, as shown in Fig. 2.7, ZmVar reflectivity for cloud liquid is higher than the COSP one of about 8 dBZ for every value of HC.

(c) Snow

In COSP and ZmVar snow properties are parametrized in a very similar way. Both assume a constant density of 0.1 g/cm^3. Also, both use a constant-intercept exponential PSD, where the concentration number N_0 is fixed to 0.03 cm^{-4}. Corresponding reflectivities are compared in Fig. 2.8. However the ZmVar reflectivities are lower by about 2 dBZ. This can be explained by a difference in the snow single particle backscattering efficiency. As shown in Fig. 2.9, the backscattering efficiency for ZmVar is at least 30% lower than for COSP. The reason for this inconsistency is in the different formula used to model the permittivity of soft ice (ice with air inclusions). ZmVar uses the formulation of Maxwell Garnett (1904), while the one of Bruggeman (1935) is used in COSP. When the Maxwell Garnett formulation is used in COSP instead of the original, differences disappear both in the single scattering (Fig. 2.9, black crosses) and in the simulated reflectivities (Fig. 2.8, black curve). As for the rain, the use of a logarithmic, rather than a linear, discretization of diameter has little impact on the calculated reflectivities.

(d) Cloud Ice

In ZmVar the same Modified Gamma PSD used for cloud liquid is assumed for cloud ice. However, COSP models the cloud ice PSD with a Gamma function, also shown in Fig. 2.10. A further difference in ZmVar is that cloud ice particles are assumed to be pure ice, while in COSP a variable size density is employed (Tab. 2.1.2) which for sizes below 0.01 cm is very close to the pure ice one. The reflectivity due to cloud ice resulting from the two operators is plotted in Fig. 2.11. We observe that the ZmVar reflectivity is smaller by about 12 dBZ for all water contents. This large discrepancy can be attributed primarily to the PSD parametrization. As shown in Fig. 2.10, in ZmVar the number of particles drops sharply for diameters above 0.005 cm, while for COSP the same happens only for sizes above 0.01 cm. Tests in the following section will show that sensitivity to density is less than for the PSD.

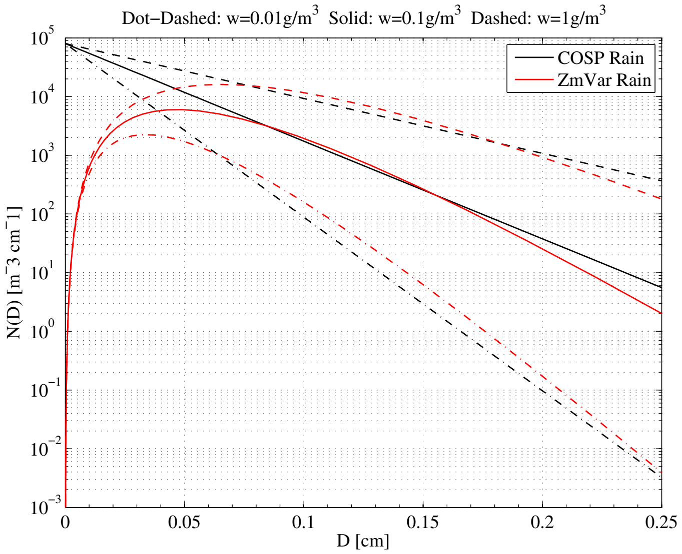

Figure 2.3: Rain PSD used in COSP and ZmVar for three values of hydrometeor content w: 0.01 $g\,m^{-3}$ (dot-dashed line), 0.1 $g\,m^{-3}$ (solid line) and 1 $g\,m^{-3}$ (dashed line).

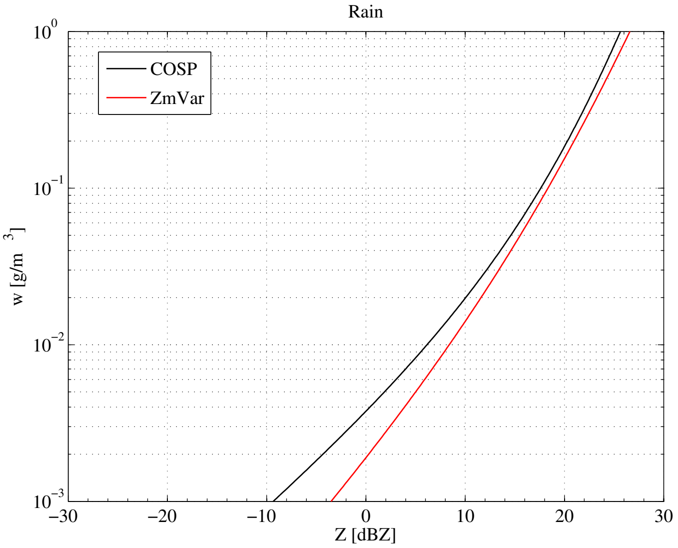

Figure 2.4: Equivalent Reflectivity as function of rain HC obtained from COSP and ZmVar.

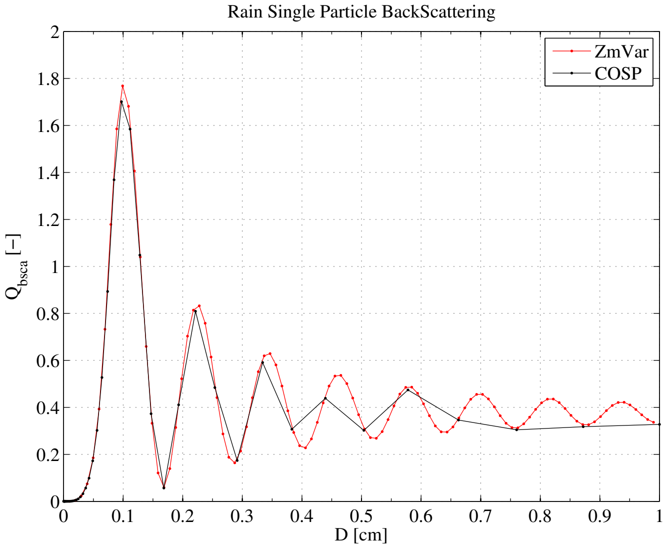

Figure 2.5: Single particle rain backscattering efficiency obtained from Mie routine in ZmVar and COSP.

2.1.4 Sensitivity to microphysical assumptions

Hydrometeor PSDs and ice density are parameters required in order to simulate reflectivities. Atmospheric models do not always explicitly provide information about them, therefore assumptions have to be made before running the simulator. In this paragraph we investigate the impact on Zs coming from PSDs and from ice density assumptions in the COSP simulator. The analysis is performed separately for each hydrometeor type.

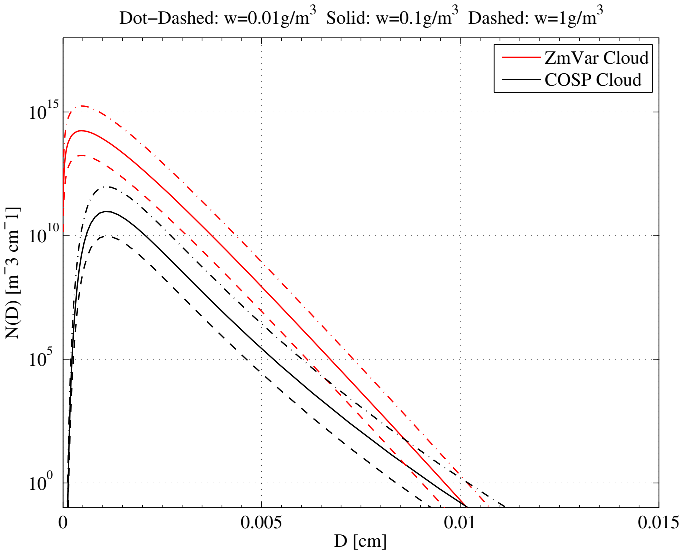

Figure 2.6: PSD used in COSP and ZmVar for cloud liquid for three values of hydrometeor content w: 0.01 $g\,m^{-3}$ (dot-dashed line), 0.1 $g\,m^{-3}$ (solid line) and 1 $g\,m^{-3}$ (dashed line).

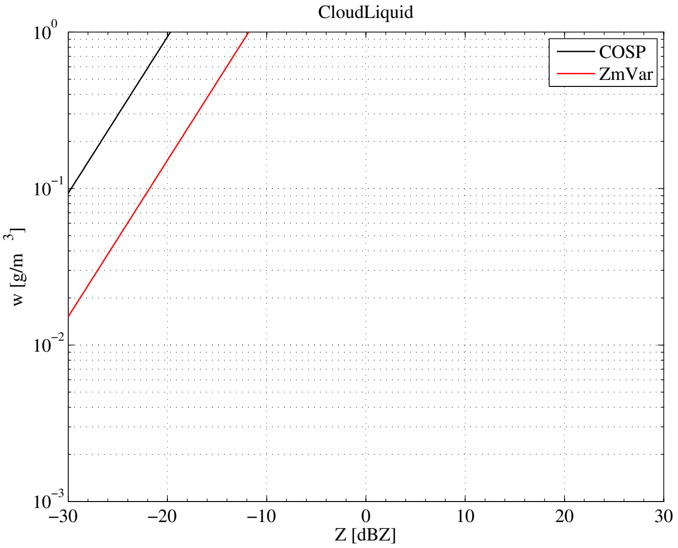

Figure 2.7: Equivalent Reflectivity as function of cloud liquid HC obtained from COSP and ZmVar.

2.1.4.1 Particle Size Distributions

Rain PSD

It is difficult to assign a globally valid PSD to rain since the raindrop spectrum is dependent on precipitation regime and climate regions. In COSP, the widely used Marshall-Palmer distribution is employed. Although this represents a good general approximation, we have investigated the sensitivity to this assumption comparing the simulated reflectivity with the ones obtained using two different PSDs, both Gamma with factor parameter ν=2, but fixing a different constant particle number concentration N_0. The values chosen give spectra that are complementary to the Marshall-Palmer one. As shown in Fig. 2.12, a first PSD (PSD1,

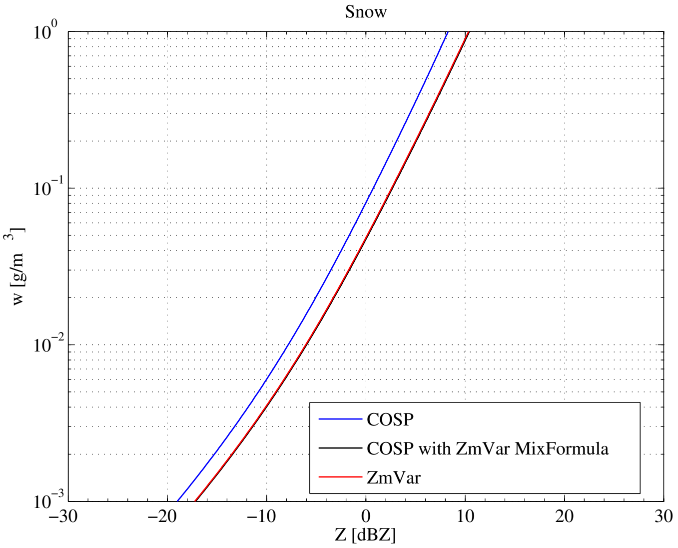

Figure 2.8: Equivalent Reflectivity as function of snow HC obtained from COSP, COSP using ZmVar effective permittivity formulation, and ZmVar.

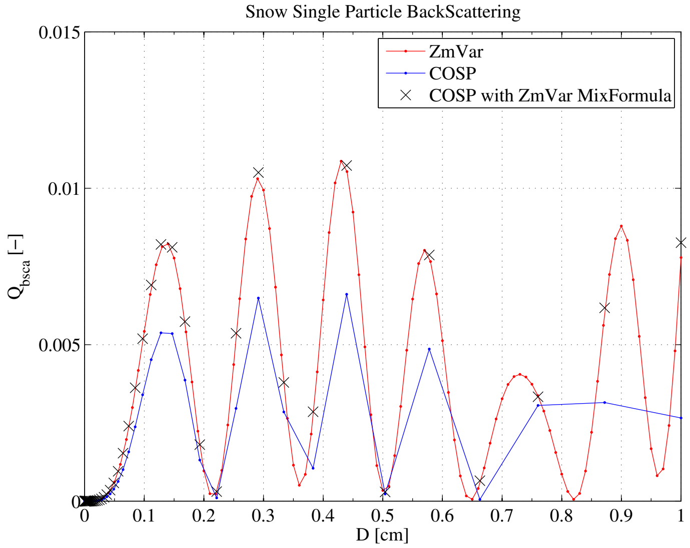

Figure 2.9: Single particle snow backscattering efficiency obtained from Mie routine in ZmVar (red curve), COSP (blue curve) and COSP using ZmVar effective permittivity formulation (cross).

blue curves) puts more particles in the lower portion of the size spectrum than the Marshall-Palmer (black curves), while the second PSD (PSD2) behaves in the opposite way, giving particles with larger size (red curves).

Fig. 2.13 shows the obtained Zs produced by rain, as function of HC, corresponding to the three PSDs. Three regions can be identified: a first for HCs greater than 1 g/m^3 (not shown), a second region between 0.1 and 1 g/m^3, and a third one below 0.1 g/m^3. In the first region PSD1 (blue curve) produces higher Zs than the Marshall-Palmer one (black curve) while PSD2 (red curve) gives lower Zs. In second region, the three cases are comparable. In the third region, PSD2 (red curve) gives Zs larger than the Marshall-Palmer

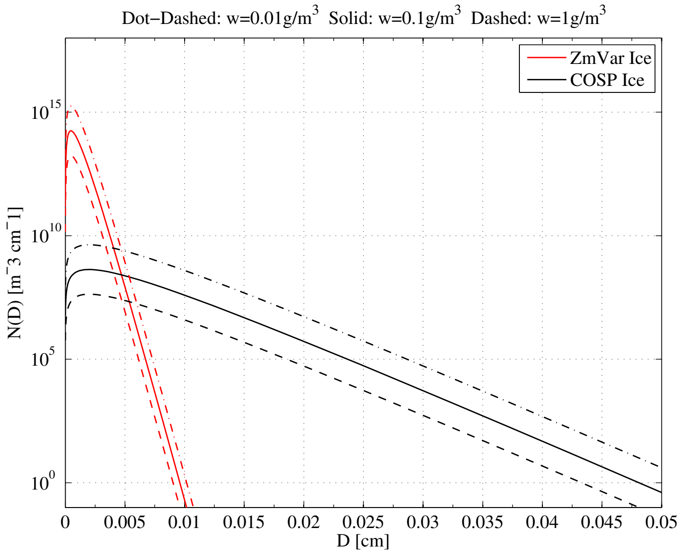

Figure 2.10: PSD used in COSP and ZmVar for cloud ice for three values of hydrometeor content w: 0.01 gm^{-3} (dot-dashed line), 0.1 gm^{-3} (solid line) and 1 gm^{-3} (dashed line).

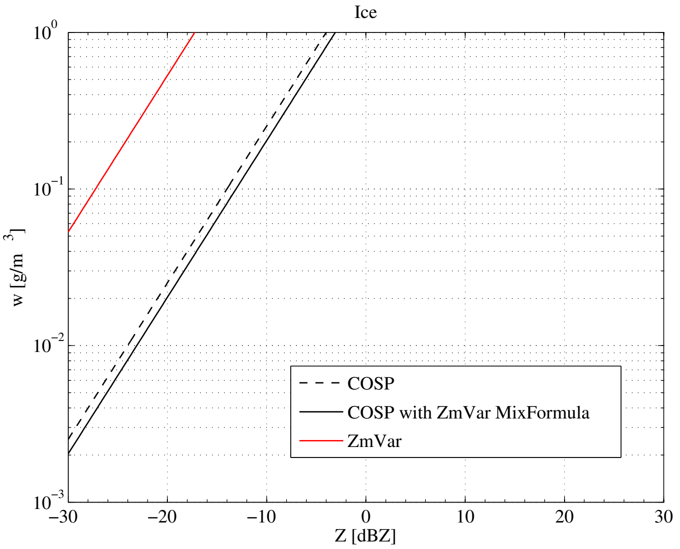

Figure 2.11: Equivalent Reflectivity as function of cloud ice HC obtained from COSP (black dashed line), COSP using ZmVar effective permittivity formulation (black solid line) and ZmVar (red line).

one, while PSD1 (blue curve) gives lower values. Comparing these results with the shapes that each PSD assumes for different HCs, we note that Z is mainly driven by particles having a diameter below 0.2 cm (see Fig. 2.5).

It is worth noticing that attenuation along the ray path is not taken into account into our calculations but attenuation can be significant for millimetre-waves. For example, for typical mid-latitude precipitation events, strong attenuation of the signal would occur for rain rates above $15-20\,mm/h$, i.e. a hydrometeor content of roughly 1 g/m^3 (Haynes *et al.*, 2009).

Cloud Liquid PSD

Sensitivity of cloud liquid to PSD has been investigated similarly as for rain, being the main source of uncertainty also in this case. The original PSD defined in COSP for cloud liquid has been compared with two monodisperse distributions: one for a drop diameter of 10 μm and another of 30 μm. These two values have been chosen since they represent typical cloud droplet sizes in some cloud types (Pruppacher and Klett, 1998, Fig. 2.11 in their book). The equivalent reflectivity as function of cloud liquid amount for each PSD is shown in Fig. 2.14. We note that the curve relative to COSP (black) lies between the ones corresponding to the two monodisperse with a constant offset of about 8 dBZ in both cases. This difference shows the importance of specifying a realistic PSD also for cloud liquid.

Snow PSD

The importance of PSD for snow has been investigated replacing the original one with the one assumed for ice in Ryan (2000). The model assumes the following exponential PSD:

$$N(D) \quad = \quad N_0 exp(-\lambda D) \tag{2.15}$$

where the number concentration intercept N_0 is constant while the inverse of the median volumetric diameter λ (m^{-1}) has a dependence on temperature (T, in C) given by:

$$\lambda(T) \quad = \quad 1220\,10^{-0.0245\,T} \tag{2.16}$$

The reduction of slope with increasing temperature is an implicit way of parametrizing aggregation and the dependence of ice nucleus concentration on temperatures. Fig. 2.15 shows the shape of this PSD for two reference values of temperature. The corresponding Zs are in Fig. 2.17. A snow density constant value of $0.1\,g/m^3$ is assumed. Using the new PSD Zs higher than the original exponential are obtained. The discrepancy increases as temperature decreases.

Cloud Ice PSD

Similarly to what is done for rain, the sensitivity of cloud ice to PSD has been tested slightly changing the PSD parameters of the one used in COSP (keeping the density formulation). In a first test the shape parameter ν has been moved from 2 to 3, and in a second test the mean diameter D_m has been increased from 40 μm to 60 μm. The impact of these changes on the PSD is shown in Fig. 2.16 (considering a HC of $0.1\,g/m^3$). Corresponding Zs are given in Fig. 2.17 (black curves). As expected, the increase in ν results in a decrease in Zs, while an increase in D_m produces an increase. In spite of the small amplitude of the changes, differences from the original setup are about $3-4\,dBZ$.

Note on Cut off

An important difference between the two simulators is in the way particle size limits are handled. In ZmVar a minimum and a maximum size are defined for each hydrometeor as input. In QuickBeam (used by COSP) the particle size is hard-coded to a range between specified minimum and maximum values which are the same for all hydrometeor types (type-specific limits are implemented only for the power law PSD). Therefore, in QuickBeam the PSD takes into account a wide range of particles sizes for the integration in Eq. (2.1) and relies on values close to zero for unrealistic sizes. In ZmVar, the fact that limits have to be specified implies that only a portion of the PSD is actually used. Consequently, care must be taken when fixing the limits, in order to avoid an unwanted truncation of the PSD in the integration of Eq. (2.1).

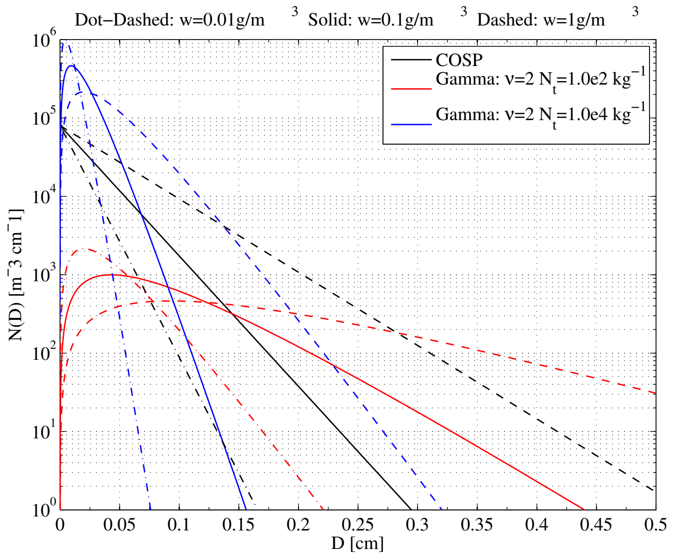

Figure 2.12: COSP rain size distribution (black lines) compared to two (blue and red) Gamma distribution with different constant particle concentration ($1.0\,e^2 kg^{-1}$ - red lines and $1.0\,e^4 kg^{-1}$ - blue lines). Distributions are shown for three values of hydrometeor content w: 0.01 $g\,m^{-3}$ (dot-dashed line), 0.1 $g\,m^{-3}$ (solid line) and 1 $g\,m^{-3}$ (dashed line).

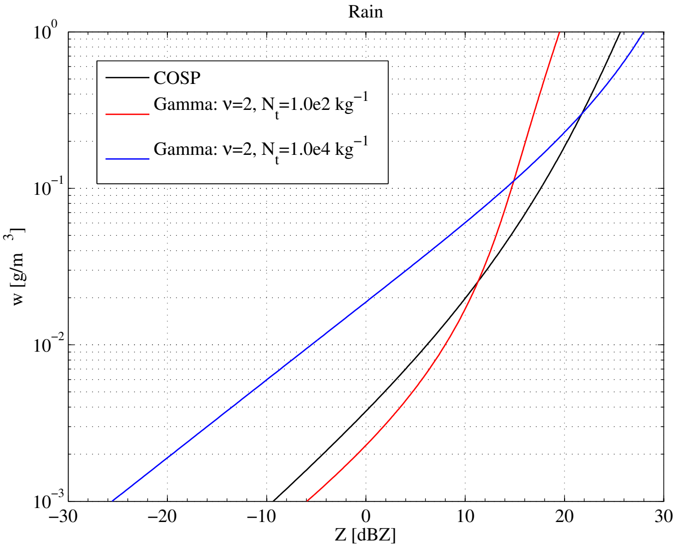

Figure 2.13: HC-Z relationship for rain using different PSDs as presented in Fig. 2.12.

2.1.4.2 Density of frozen particles

Ice can assume a variety of shapes/densities depending on the growing environment and on the evolution of the single particle. Modelling of frozen particles density is therefore not easy since it is difficult to define a unique value always appropriate. Given the complexity, many studies have tried to model the ice shape starting from *in situ* measurements. One of these is the expression suggested for snow by Brown and Francis (1995) which it is given in Fig. 2.18 together with the ones used for cloud ice and snow in COSP.

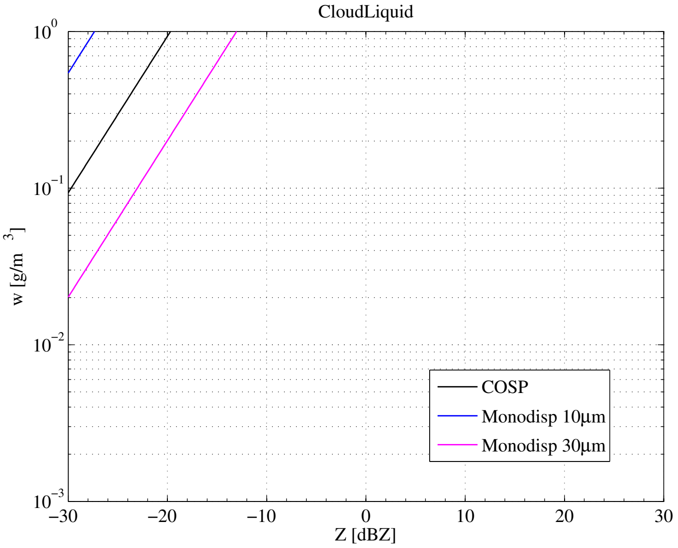

Figure 2.14: HC-Z relationship for cloud liquid using different PSDs: COSP (black line) and two monodisperse distributions for a drop diameter of 10µm (blue line) and of 30µm (red line).

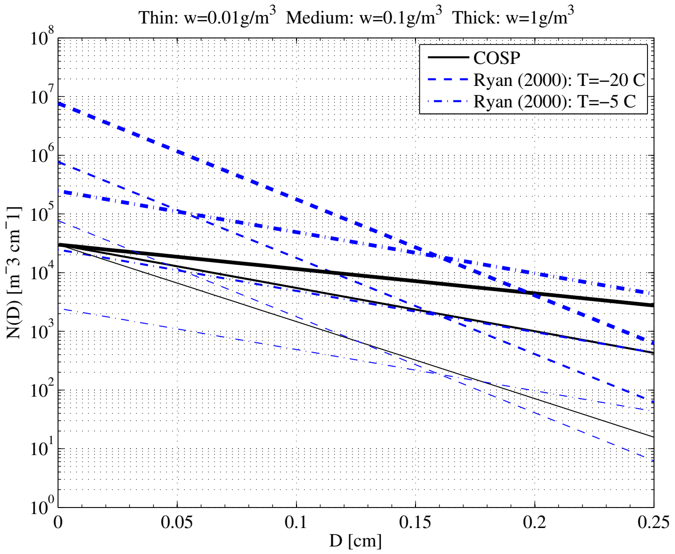

Figure 2.15: COSP snow size distribution (black lines) compared to the distribution in Ryan (2000) for two reference values of temperature (-20 C: blue dashed lines and -5 C: blue dot-dashed lines). Distributions are shown for three values of hydrometeor content w: 0.01 $g\,m^{-3}$ (dot-dashed line), 0.1 $g\,m^{-3}$ (solid line) and 1 $g\,m^{-3}$ (dashed line).

Snow density

For falling ice (snow), the critical parameter can be identified in its density since this is highly variable. In COSP a size independent constant density of $0.1\,g/cm^3$ is assumed for snow. However, several expressions have been proposed to parametrize snow density as a function of size. Widely used is the one of Brown and Francis (1995) (red curve in Fig. 2.18) which has been derived from *in situ* measurements. In Fig. 2.19, Zs evaluated using COSP density are plotted together with the ones obtained using Brown and Francis relationship. Zs using this new density expression (blue dashed line) are significantly lower than the ones obtained using the constant value (blue solid line). Difference increases as HC increases, up to 5-8 dBZ.

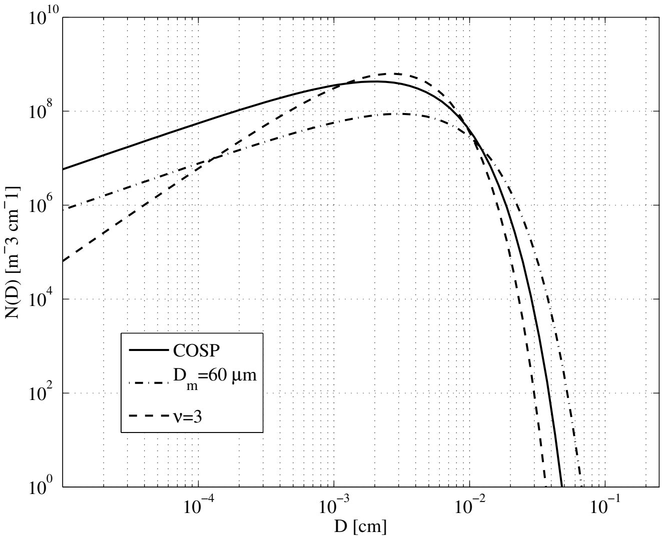

Figure 2.16: Cloud ice size distribution in the original COSP (solid line), after changing the mean diameter Dm from 40 μm to 60 μm (dot-dashed line) and after changing the shape parameter ν from 2 to 3 (dashed line).

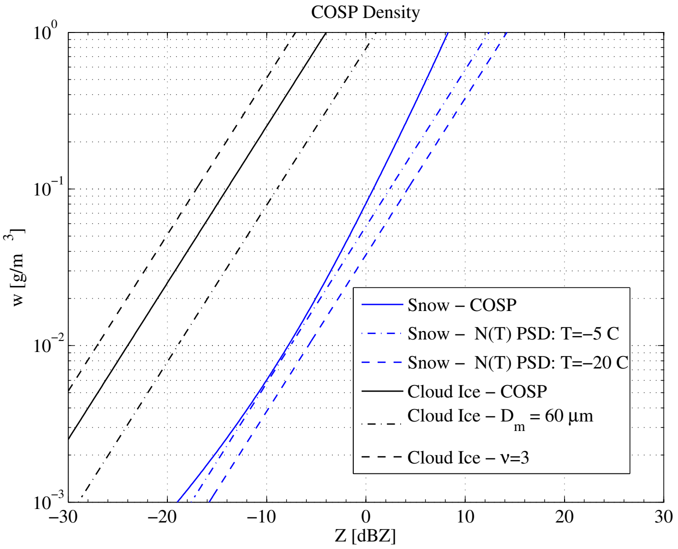

Figure 2.17: HC-Z relationships using different PSDs presented in Figs. 2.15 and 2.16. Blue curves are for snow and black for cloud ice.

Cloud Ice density

The density expression for cloud ice implemented into COSP is also shown in Fig. 2.18 (black line with dots): it prescribes the value of pure ice for the smallest diameters and quickly approaches (at around 50 μm) an asymptotic value of about 0.4 g/m^3. The impact of density choice on Z is investigated changing the original with two constant values: one very high ($0.91\,g/cm^3$, pure ice) and one quite small ($0.25\,g/cm^3$). Fig. 2.19 shows (black lines) that the COSP original one lies between the other two (dashed and dot-dashed black lines), with an offset of $3-4\,dBZ$.

Note on Soft Ice

There is not a unique way to evaluate the optical properties of a particle having a density less than the one of pure ice (soft ice). Within COSP/QuickBeam two alternative options are implemented. The first considers each particle as a sphere of solid ice that has a new (smaller) effective diameter which conserves the particle mass. The second keeps the diameter specified by the mass and assumes an effective density (lower than the one of solid ice). Therefore each frozen (ice and snow) particle is modelled as a 'spongy' sphere composed of a mixture of ice and air having an effective permittivity (e.g. Bruggeman, 1935). Fig. 2.20 shows, for different density values, the single-particle backscattering efficiency $Q_{\mathrm{bs}} = \sigma_{bs} / \left(\pi D^2 \right)$ as function of diameter for the two formulations. The equivalent-solid approach (dashed lines) always provides higher values that the soft-ice one (solid lines). Differences increase as particles become larger, in line with what is shown in Liu (2004) for the particle (omni-directional) scattering. Interestingly, for a given diameter, Q_{bs} doesn't always increases as density increases. This means that the equivalent (smaller) pure ice particle can be a less efficient scatterer than the 'soft' one.

Zs resulting from using the equivalent-solid approach for snow and cloud ice are plotted in Fig.2.21. For snow (blue lines), the simulated Zs are larger, with differences increasing as HC increases ($10\,dBZ$ for HC of 1 g/m^3). For the cloud ice (black lines), Zs evaluated using the equivalent-solid method are only slightly lower (less than $0.5\,dBZ$) than the ones obtained using the soft-ice approach. This can be attributed to the smaller size and higher density of cloud ice particles than the snow ones.

2.1.4.3 Summary on sensitivity tests

From the simple sensitivity tests shown above, the following quantities emerged as the main sources of uncertainties:

- Particle size distributions for cloud liquid and rain are highly variable and therefore difficult to model. For both, tests showed a strong sensitivity to PSD, particularly for rain.
- When considering frozen particles, there is also the uncertainty on density. Tests showed that reflectivity is very sensitive to snow density, while the PSD is the most important parameter for cloud ice.

2.1.5 Changes to ZmVar and comparison with observations

The comparison of reflectivity values simulated by ZmVar with the ones from COSP separately for each type of hydrometeor has shown non-negligible discrepancies. Differences stem from the simpler assumptions made in ZmVar in specifying PSDs and from the differences in modelling the density of frozen particles.

The following changes are proposed for ZmVar.

- For rain, use the Marshall-Palmer PSD (as in COSP). This brings small differences in Zs, but has the advantage of having a widely used distribution.
- For cloud liquid, use the same PSD as in COSP. In the previous section emerged that cloud liquid reflectivities in ZmVar are much higher than COSP. Comparison with results available in the literature (e.g. Clothiaux *et al.*, 1995, Fig. 9) shows that the ZmVar values are too high, while the COSP ones agree quite well.

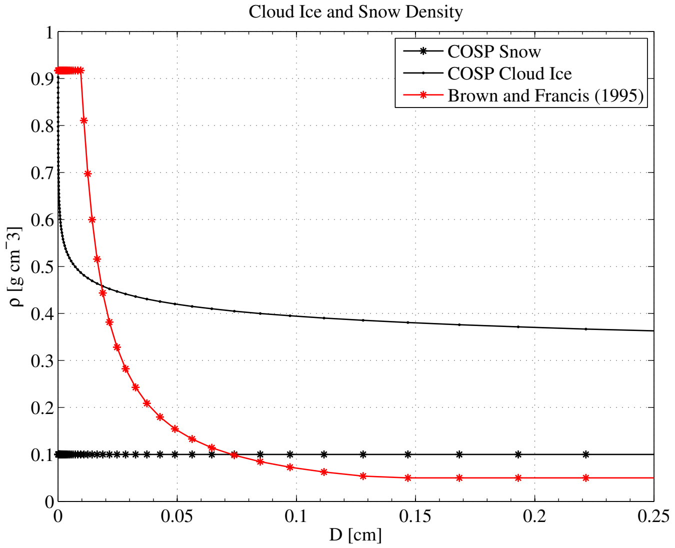

Figure 2.18: Snow and Cloud Ice density-size relationships as used in COSP for snow (black line with stars), COSP for cloud ice (black line with dots) and as suggested by Brown and Francis (1995) (red line with stars).

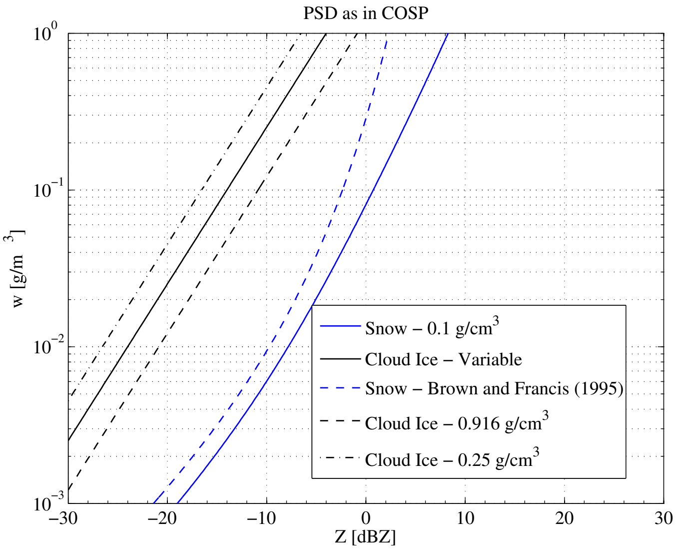

Figure 2.19: HC-Z relationships using different ice densities and PSDs in COSP. Blue curves are for snow and black for cloud ice.

- For cloud ice, use the same PSD used in COSP. The original PSD, being the same as used for the cloud liquid, resulted in very small sizes for cloud ice and therefore very small reflectivities.
- Cloud ice density as in COSP. Although not having the strongest impact, a variable density with size (soft ice) is a better assumption than assuming solid ice and scaling the size distribution correspondingly.

Fig. 2.22 shows the $Z-w$ relationships before and after the modifications. In particular, the changes for cloud ice bring the relationships in ZmVar for cloud ice (and also snow) closer to similar ones derived in

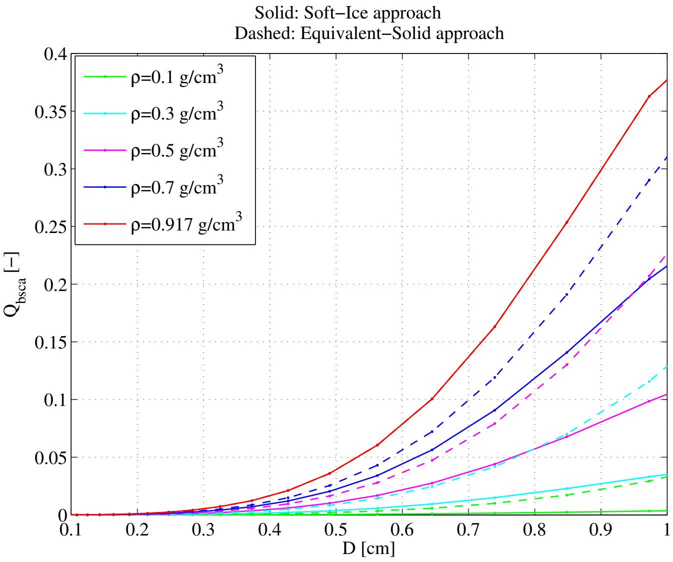

Figure 2.20: Single particle ice backscattering efficiency as function of size. Colours are for different density values. Solid lines are for the soft-ice and dashed for the equivalent solid approach.

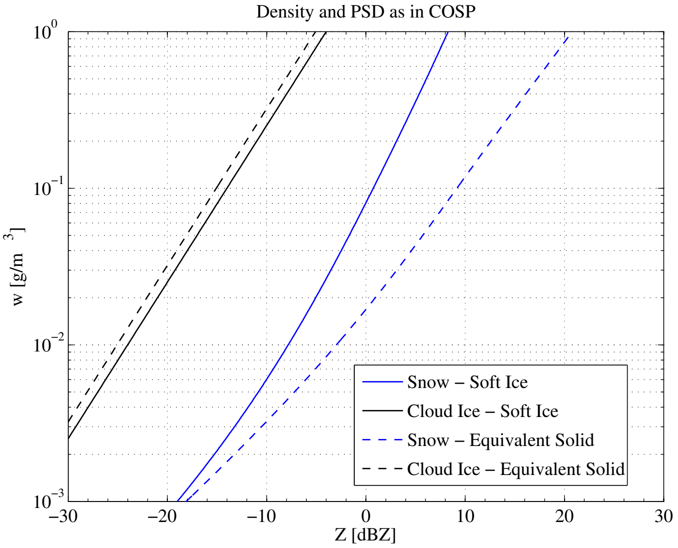

Figure 2.21: HC-Z relationships using soft ice (solid lines) and equivalent solid approaches (dashed lines). Blue lines are for snow and black for cloud ice.

Hong *et al.* (2008) from *in situ* measurements.

The comparison also indicated some potential improvements for QuickBeam.

- A linear spacing for the particle size binning instead of logarithmic could avoid possible aliasing of Mie effects (although impacts are shown to be small).
- The ice permittivity model of Warren (1984) could be update according to Warren and Brandt (2008). In their work they included the results of Mätzler and Wegmüller (1988) which were based on newer available measurements. In ZmVar, the latter model is already employed.

- The gas absorption model of Liebe (1985) should be update with the one of Liebe *et al.* (1992) as in ZmVar.

The impact of the modifications on the final values of simulated reflectivities can be investigated running ZmVar using a new Mie-table generated including the proposed changes to ZmVar. For this purpose, a set of adjacent profiles has been extracted from the ECMWF model that corresponds to a cloudy and precipitating situation. The vertical cross section of HCs for the selected profiles is shown in Fig. 2.23. Corresponding reflectivities generated using ZmVar with the new Mie-table are in Fig. 2.24 (top panel). The difference with the reflectivities obtained using the original set up are plotted in the same figure (bottom panel). We note that below the freezing level, the new setup produces always lower Zs. This is consistent with the fact that liquid hydrometeors in the scheme give lower Zs for the same amount of content. Again consistently with the changes to the Mie-table, we also note that larger differences (5 dBZ or more) correspond to low values of Z, where more cloud liquid than rain is present. Above the freezing level changes are less pronounced (between -1 and 1 dBZ). The increase in reflectivity due to the new cloud ice parametrization is hidden almost everywhere by the co-existence with snow, having a stronger negative signal.

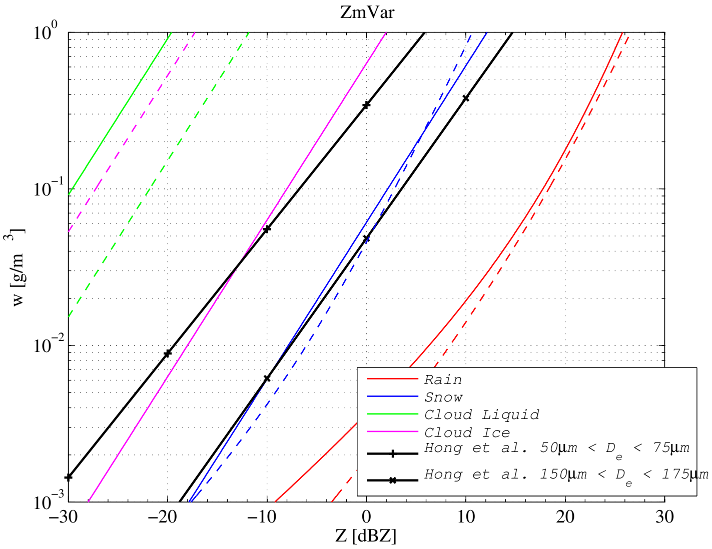

Figure 2.22: HC-Z relationships for each of the hydrometeors of interest resulting from ZmVar. Dashed lines are for the original version, solid for the updated version.

2.2 Treatment of cloud fraction

Global circulation models, given their coarse horizontal resolution, need a sub-grid (horizontal) representation of cloud fraction (while they are supposed to fill the gridbox in the vertical). Consequently, assumptions must be made on how clouds overlap in the vertical within a grid column. The particular choice of these assumptions has an impact on the evaluation of atmospheric radiation and on the reflectivity. In this section, the treatment of cloud fraction in ZmVar is compared with the one implemented in COSP and the differences of simulated Zs are evaluated.

2.2.1 ZmVar

The way ZmVar takes into account cloud fraction involves the following steps:

1) For each layer l, the model specifies the cloud fraction F_l^C only for cloud liquid and cloud ice. ZmVar assigns a precipitation fraction F_l^P to rain and snow starting from F_l^C and makes the assumption of random

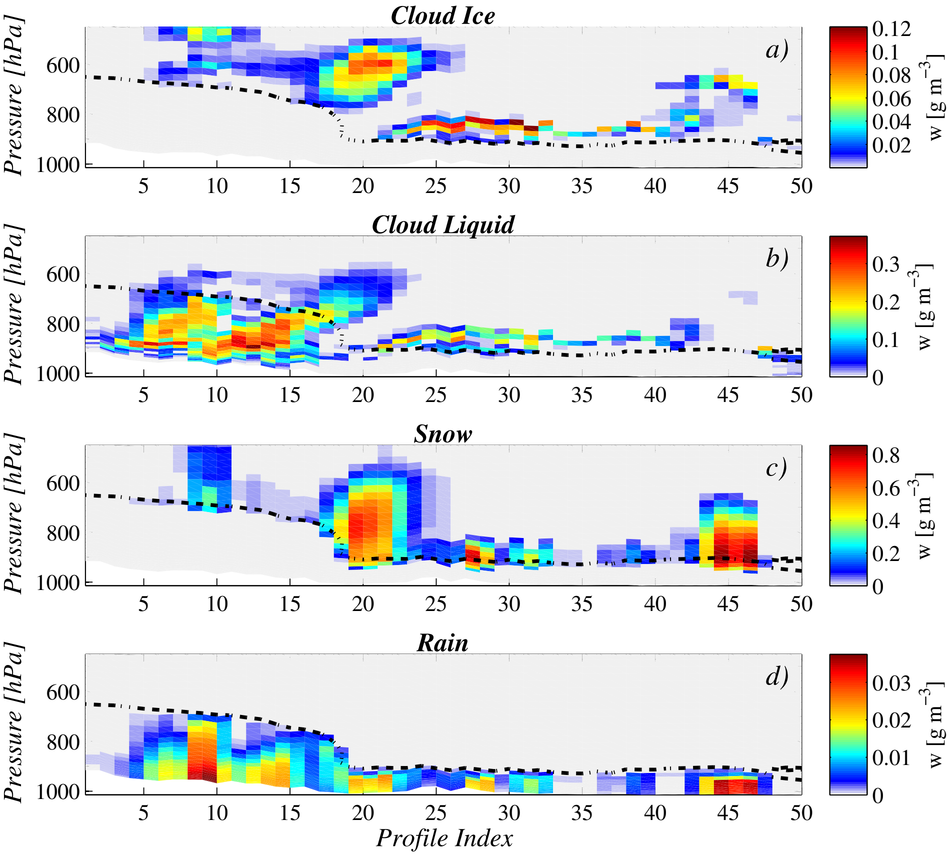

Figure 2.23: Cross section of cloud profiles as extracted from the global ECMWF model forecast. From top to bottom: HC of cloud ice, cloud liquid, snow, and rain. Dashed line shows the height of the freezing level.

overlap for precipitating hydrometeors:

$$F_l^P = 1 - \prod_{i=1}^{l}(1 - F_i^C) \tag{2.17}$$

2) The in-cloud value of content w'^h_l at layer l for hydrometeor h is evaluated from the box-average values given by the model scaling according to the corresponding fractions:

$$w'^h_l = \frac{w_l^h}{F_l^h} \tag{2.18}$$

where F_l^h is F_l^C for cloud liquid and cloud ice and F_l^P for rain and snow.

3) The in-cloud reflectivity Z'^h_l and extinction β'^h_l are then evaluated using w'^h_l, as described in Section 1.1. Grid box averages Z_l and β_l are then obtained 'scaling back' the in-cloud values according to the cloud and precipitation fractions and summing on the total number of hydrometeors N_{HYD}.

$$Z_l = \sum_{h=1,N_{\text{HYD}}} F_l^h \, Z_l^h \tag{2.19}$$

$$\beta_l = \sum_{h=1,N_{\text{HYD}}} F_l^h \, \beta_l^h \tag{2.20}$$

It is interesting to note that the values of β_l^h are very similar to the ones corresponding to the (unscaled) w_l^h

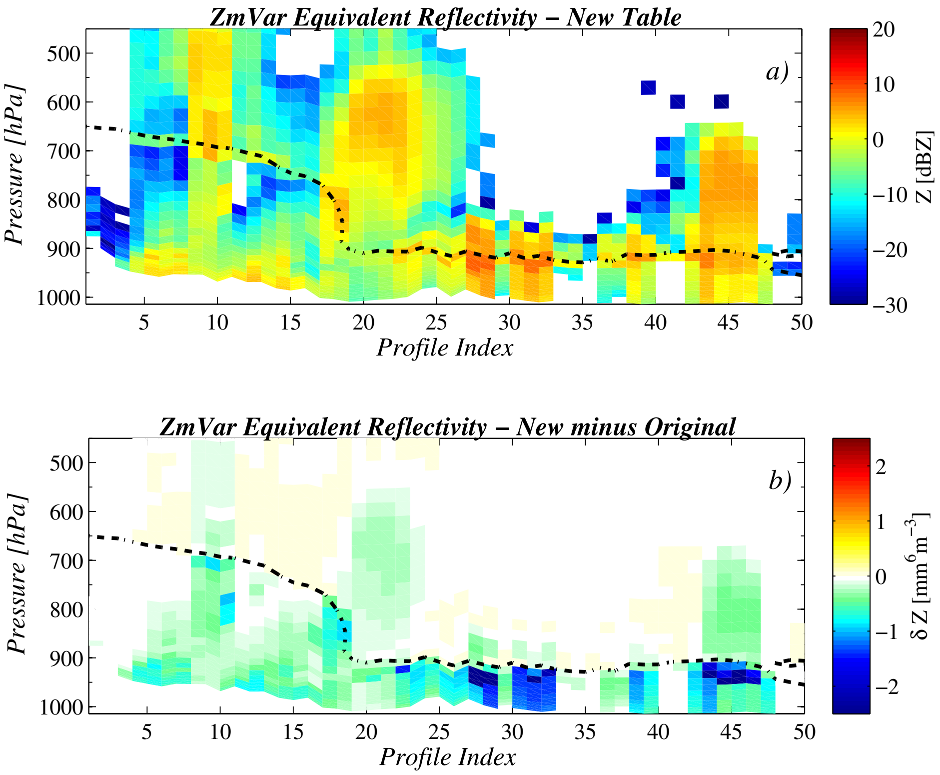

Figure 2.24: Top panel: ZmVar simulated 94 GHz radar reflectivity using the Mie look-up table with the modifications described in the text. Bottom panel: differences with the reflectivities obtained using the original table.

since, as shown in Fig. 2.25, for all hydrometeors, extinction coefficients have a (quasi-) linear dependence on hydrometeor content.

4) Finally, the reflectivity measured by the radar Z^a is evaluated taking into account the attenuation along the path:

$$Z_l^a \;=\; Z_l\, e^{-2\bar{\tau}_l} \tag{2.21}$$

where $\bar{\tau}_l$ is the average optical depth between the l-th layer and the top of the atmosphere defined as:

$$\bar{\tau}_l \;=\; \sum_{i=1,l} \sum_{h=1,N_{\mathrm{HYD}}} F_i^h\, \beta_i^h\, \Delta h_i \tag{2.22}$$

where $\Delta h_i$is the depth of the i-th layer. We note that in this approach no information is needed about the way clouds overlap vertically within the box.

2.2.2 COSP

Cloud overlap is treated in COSP using the Subgrid Cloud Overlap Profile Sampler (SCOPS) , part of the International Satellite Cloud Climatology Project (ISCCP) simulator (Webb *et al.*, 2001). This package uses a pseudo-random sampling process to generate an ensemble of sub grid clouds and precipitation profiles representing the distribution within the model grid box. It takes vertical profiles of cloud/precipitation amount and cloud fraction as input to generate a specified number of horizontally homogeneous cloud/precipitation profiles.

Three schemes of cloud overlap are available within SCOPS, namely random, maximum and maximum-random. The most basic formulations of cloud overlap are ”maximum” or ”random” and the most commonly

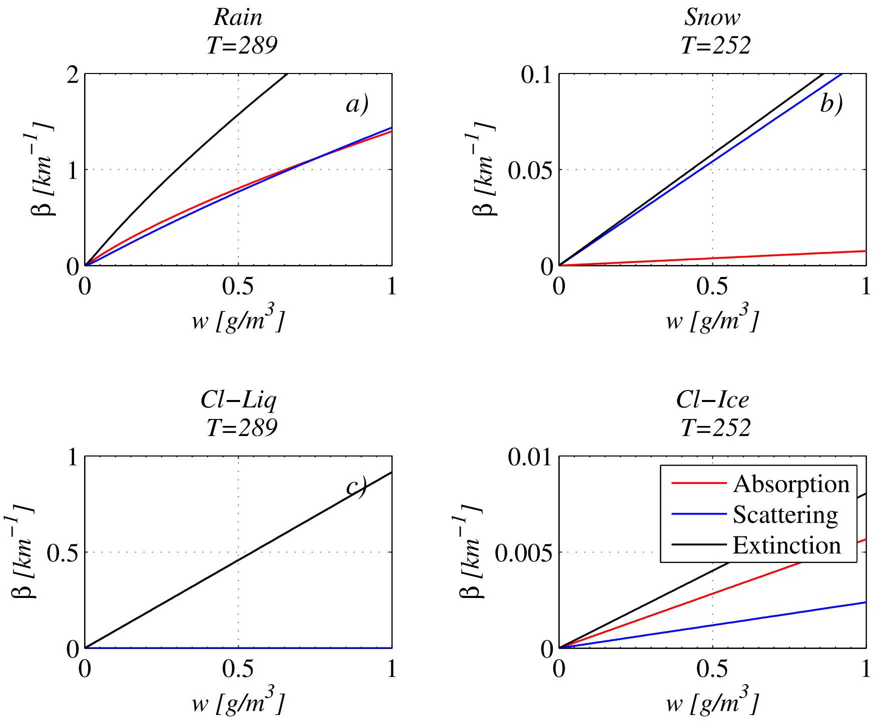

Figure 2.25: Typical volumetric extinction, absorption and scattering dependence on HC for rain, snow, cloud liquid, and cloud ice.

used overlap is ”maximum-random”. The total cloud cover described by the maximum overlap assumption is simply the maximum cloud fraction in the column. Random overlap assumes that clouds at different levels are randomly overlapped with each other, so the total cloud cover will be higher than for the maximum overlap assumption. The maximum-random overlap assumption applies the maximum overlap within a vertically coherent cloud block, but random overlap between vertically non-adjacent cloud blocks. This assumption was the most consistent with a statistical analysis of observed cloud distributions described by Tian and Curry (1989) and has been widely used in GCMs. A description of each scheme can be found, among others, in Raisanen *et al.* (2004).

The SCOPS algorithm splits each grid column into a number of sub-columns N_{COL} in which each layer is either completely filled or completely free with cloud. The cloud cover $F'^{C}_{l,k}$ in the l-th layer of the k-th sub-column is therefore either 0 or 1.

In the maximum random overlap case, two arrays $\boldsymbol{x}$ and $\boldsymbol{y}$ are generated containing uniformly distributed random numbers between 0 and 1. They define the probability that cell l of sub-column k is cloudy or clear as follows.

A threshold $t_{l,k}$ is first evaluated as:

$$t_{l,k} = \begin{cases} x_{l,k} & \text{if } x_{l,k} < \min(F_l^C, F_{l-1}^C) \\ \min(F_l^C, F_{l-1}^C) + y_{l,k}[1 - \min(F_l^C, F_{l-1}^C)] & \text{if } x_{l,k} \geq \min(F_l^C, F_{l-1}^C) \end{cases} \tag{2.23}$$

The cloud cover is then assigned accordingly:

$$F'^{C}_{l,k} = \begin{cases} 1 & \text{if } F_l^C > t_{l,k} \\ 0 & \text{if } F_l^C \leq t_{l,k} \end{cases} \tag{2.24}$$

where F^C_l is the grid box cloud fraction for the $l-$th layer. Note that $t_{l,k}$ is always set to zero for the top layer (l=1). It can be shown that the average cloud fraction over the sub-columns converges to the original grid box value:

$$\frac{1}{N_{\mathrm{COL}}}\sum_{k=1}^{N_{COL}} F'^{C}_{l,k} = F^C_l \tag{2.25}$$

The presence of precipitation in each sub-column layer $F^P_{l,k}$ is decided in a deterministic way from the cloud profile as obtained with the procedure described above. For layer l of sub-column k $F'^P_{l,k}$ is set to 1 if there is some precipitation in the layer and $F'^C_{l,k}$ or $F'^P_{l-1,k}$ are 1. The attenuated reflectivity for layer l averaged across all sub-columns Z^a_l in case of multi-columns can be written as:

$$\tag{2.26}$$

$$\begin{aligned} Z^a_l &= \frac{1}{N_{\mathrm{COL}}}\sum_{k=1,N_{\mathrm{COL}}} Z^a_{l,k} \qquad (2.27)\\ &= \frac{1}{N_{\mathrm{COL}}}\sum_{k=1,N_{\mathrm{COL}}}\left(\sum_{h=1,N_{\mathrm{HYD}}} F'^h_{l,k}\, Z'^h_{l,k}\right) e^{-2\tau'^{`}_{l,k}} \\ \text{where :} & \\ \tau'_{l,k} &= \sum_{i=1,l}\sum_{h=1,N_{\mathrm{HYD}}} F'^h_{i,k}\beta'^h_i\, \Delta h_i \end{aligned}$$

and $F'^h_{l,k}$ is again $F'^C_{l,k}$ or $F'^P_{l,k}$.

2.2.3 Analysis of single-column and multi-column approaches

The ZmVar simulator has been extended to include the SCOPS multi-column (MC) approach as alternative option to the original treatment single-column (SC) of cloud fraction. It is important to note that, apart from numerical issues, the two approaches produce the same grid box average un-attenuated reflectivity. Differences are only found for the attenuated reflectivity Z_a as a result of how the optical depth (from the height bin to the top of the atmosphere) is treated.

A set of experiments were run to investigate differences in the two methods. To understand (in a qualitative way) the consequence of using either of the two methods it is instructive to evaluate the attenuated reflectivity in two simplified cases. In a first example, a single-layer profile of height Δh having cloud fraction equal to 0.5 is considered (Fig. 2.26). Panel a) shows the MC approach (performed with two sub-columns), while Panel b) shows the SC. Z' and β' are the in-cloud values of volumetric extinction and backscattering, respectively. Applying Eqs. 2.21 and 2.22, the following expressions are obtained for Z_a :

$$\begin{aligned} Z^a_{single} &= 0.5\, Z^{`}\, e^{-\beta^{`}\,\Delta h} \qquad (2.28)\\ Z^a_{multi} &= 0.5\, Z^{`}\, e^{-2\beta^{`}\,\Delta h} \qquad (2.29)\end{aligned}$$

Comparing these two expressions we see that $Z^a_{single} > Z^a_{multi}$, because the scaling reduces the effect of in-box attenuation (because of the non linearity between extinction and attenuation factor) and therefore the backscattering is enhanced. Also, we note, as a special case, that when using the multi-columns the reflectivity Z' (and Z_a) could be completely attenuated (by β' within the subcolumn S_1).

The second schematic example is shown in Fig. 2.27. In this case the profile consists of two layers: one with cloud fraction equal to one and a second layer on top with cloud fraction equal to 0.5. As in the previous case, the subgridding is performed considering two sub-columns (Panel a)). Using again Eqs. 2.21, 2.22 and 2.26, the reflectivity from the bottom layer in the two approaches is equal to:

$$Z^a_{single} = Z^{'} \, e^{-2\beta^{'}_2 \, \Delta h_2} [e^{-\beta^{'}_1 \, \Delta h_1}] \quad (2.30)$$

$$Z^a_{multi} = Z^{'} \, e^{-2\beta^{'}_2 \, \Delta h_2} [0.5 + 0.5 \, e^{-\beta^{'}_1 \, \Delta h_1}] \quad (2.31)$$

In this case $Z^a_{single} < Z^a_{multi}$ because SC enhances the effect of attenuation (through the scaling and the total overlap). An important special case is where Z_a from the SC approach is completely attenuated, but the MC approach is able to still give a signal through the sub-column S_2.

The same behaviour shown in the two examples above can be observed when considering atmospheric profiles extracted from the IFS model. Fig. 2.28 shows a vertical cross section used as a case study representing light-to-moderate mid-latitude precipitation characterized by partial cloud fraction. On these profiles, ZmVar was run both in SC and MC modes (setting the number of subcolumns to 100). In the SC run the original precipitation fraction (defined in Eq. 2.17) was replaced with the one produced by MC (mean value). This makes the two experiments consistent, and therefore isolates the impact of the multi-columns or scaling approaches on Z_a. Resulting differences are shown in Fig. 2.29. Panels b) and c) show that the two methods give qualitatively similar Z_a, but the single-column provides usually higher reflectivities. Important differences of opposite sign are evident in the area between profiles 5 and 15 below 800 hPa: this region corresponds to intense rain and partial precipitation fraction. As shown in Panel a) of Fig.2.29, some of the sub-columns generated by multi-columns can be very intense and can extend very high (Z_a heavily attenuated), but some are shorter and therefore not attenuated (high values of Z_a). As mentioned above, the SC approach, using a box average attenuation can't take into account this effect (because of the lack of overlap) and therefore overestimates the effect of attenuation on Zs. As shown in the bottom panel of Fig. 2.29, this occurs only when the attenuation along the path is substantial. In the same figure, comparing again panels b) and c), we observe large regions where the opposite effect occurs: the SC approach gives slighter higher values for Z_a from profile 30 onwards and between profiles 5 and 15 (above 800 hPa). In these profiles with partial cloud fraction the total attenuation is low and the effect of the different treatment of attenuation within the box prevails.

Another way of showing these effects is through histograms. A large dataset of cloud profiles has been extracted from the ECMWF forecasts matching model grid box with CloudSat observations. All orbits of one day (3 February 2007) were used. Only precipitating profiles with $F^P < 1$ at some level were selected. F^P and not F^C was considered because the contribution to the measured Z from cloud liquid and cloud ice is small in presence of precipitation (rain or snow) and therefore the impact of their cover fraction is also negligible. About 15000 profiles were gathered in this way, representing different typical cloud structures. Fig. 2.30 shows the mean differences in Z_a using ZmVar in single-column mode and using it in multi-columns mode (25 columns), stratified for total path attenuation and precipitation fraction. The left panel is for model level 91 (i.e. the closest to surface), while the right one refers to model level 75, corresponding approximately to 800 hPa. In both plots, three main regions can be identified: a first one where differences are negligible, a second one where the SC is higher than the MC, and a third one where the opposite occurs. The SC is higher when the total attenuation is small (difference increases as F^P decreases). Conversely, MC is higher when attenuation is high enough: in this case the total-overlap assumption plays the major role. It occurs for $F^P > 0.6$ because high attenuation/precipitation is usually associated with high precipitation fraction. When considering a higher model level (right panel in Fig. 2.30), we note that there are less cases where MC is higher and they are more moderate, while in the cases where SC is higher (low attenuation) differences are more pronounced.

A summary of the differences between the two approaches is shown in Fig. 2.31, where the differences in Z_a are plotted for each model level from top to approximately 980 hPa (level 85 of 91-level model). The mean difference between SC and MC is positive (Panel a)), indicating that on average the effect of the attenuation within the same box of the reflectivity is dominating, leading to a positive bias of almost 0.4 m^6mm^{-3} (≈ -4 dBZ) up to level 65.

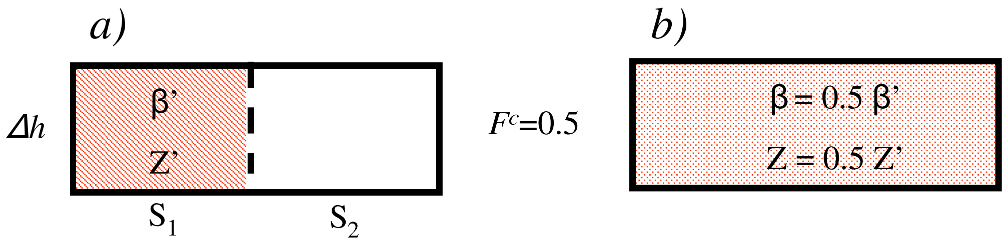

Figure 2.26: Schematic representation of a single layer profile with partial cover for multi-column (a) and single-column (b) approaches. See text for explanation.

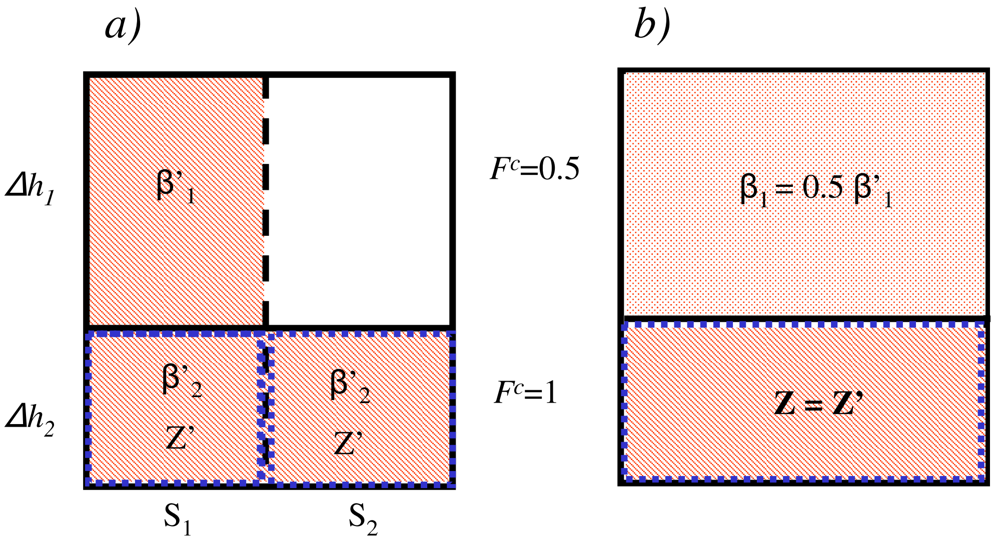

Figure 2.27: Same as in Fig. 2.26, but for a schematic representation of a two-layer profile. See text for explanation.

2.2.4 Performance of single-column and multi-column approaches

The minimum number of sub-columns in the MC approach required to get a box-average reflectivity accurate enough can be investigated testing the dependence of box-average reflectivity Z^a on the number of columns (convergence). Fig. 2.32 shows the absolute difference between Z^a obtained using the number of columns indicated in abscissa and a reference of 300 columns. The global dataset of 15000 profiles described above has been used. In the same figure, the difference between the SC and the reference is also reported (red line). We note that the MC method using few columns already gives two times smaller the mean difference compared to the single-column. The difference with the reference in the MC method decreases sharply from 20 to 30 sub-columns and reaches a sort of asymptotic value around 50 columns. This result suggests 30-40 columns as reasonable number.

The corresponding computational cost is given in Tab. 2.1, which reports the CPU time (Pentium 4 @ 3.4

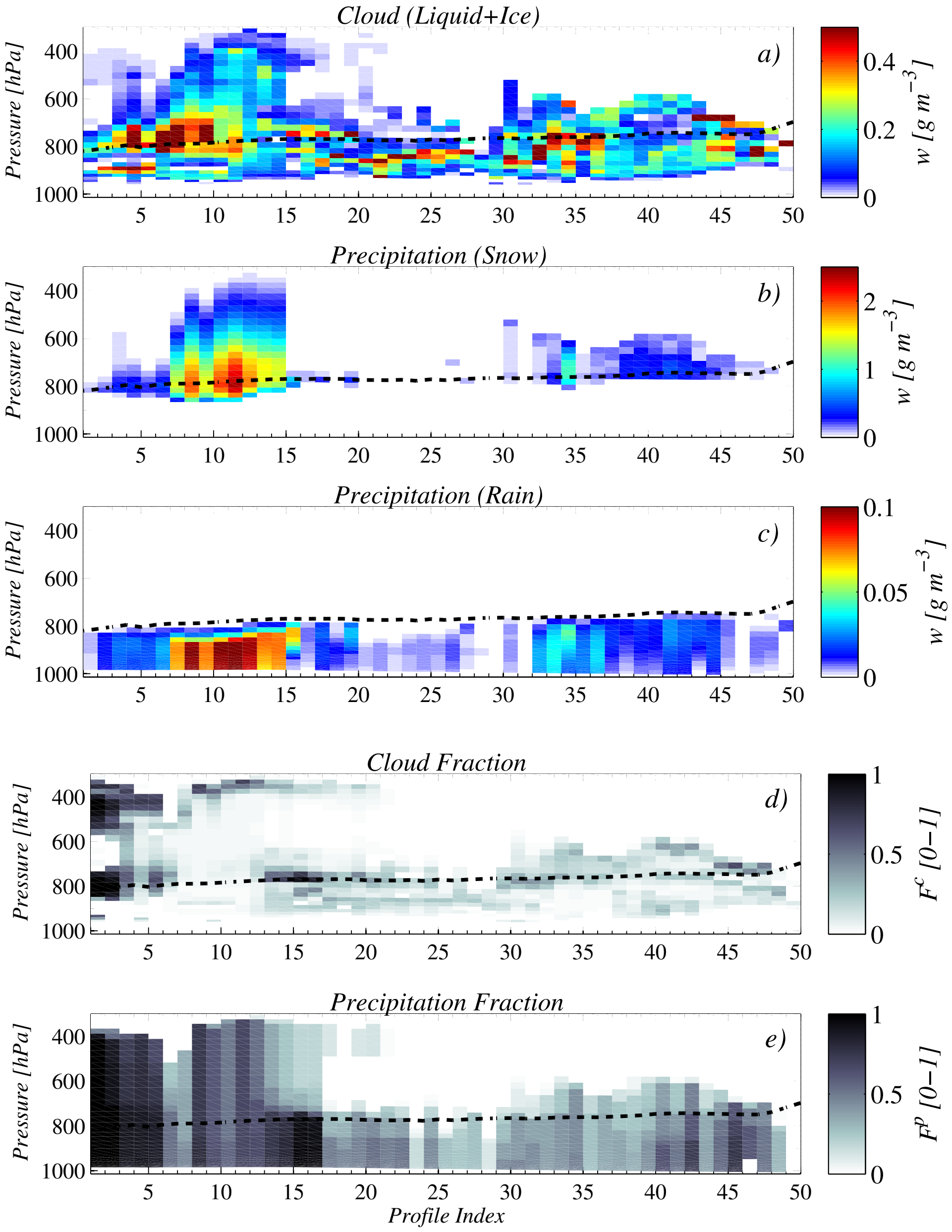

Figure 2.28: Vertical cross section of IFS model profiles corresponding to a precipitation event.

GHz) for different number of sub-columns. The cost remains quite small for reasonable numbers (e.g., about 7% increase for 30 columns) then increases linearly with the number of columns.

2.2.5 Comparison with observations

In Section 2.2.3, the differences between the single-column and multi-column approach were investigated. To demonstrate that the MC mode constitutes a better model, it is necessary to check if it brings the simulations closer to real observations. The evaluation of differences between model and observations is possible using the model profiles extracted in correspondence with CloudSat observations. Reflectivity profiles

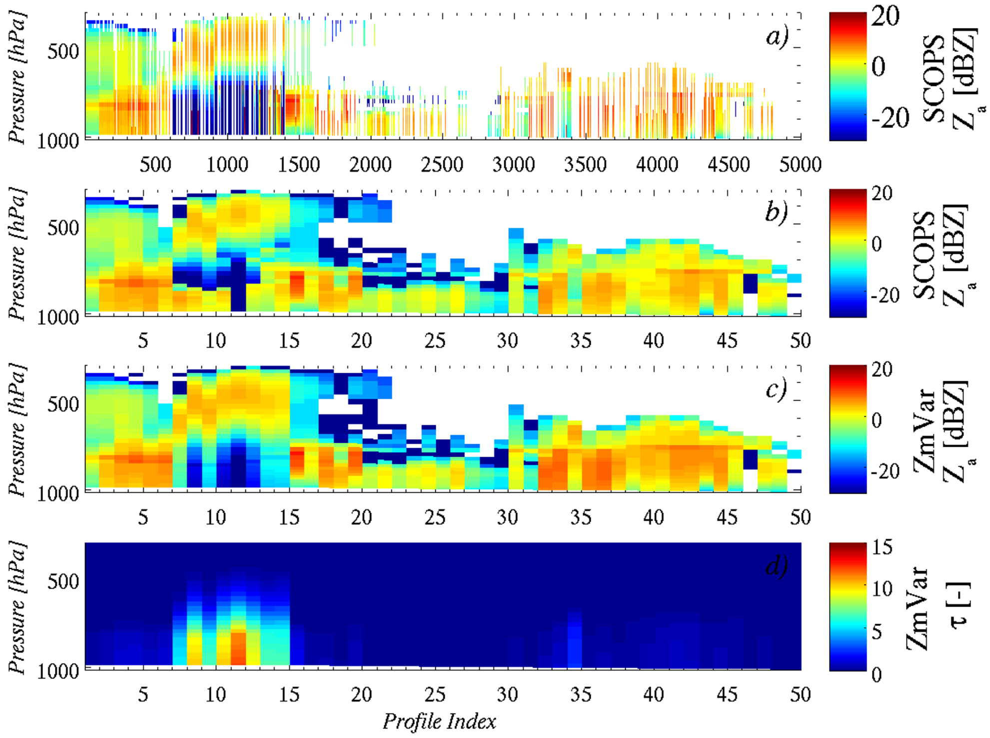

Figure 2.29: ZmVar simulations using profiles from Fig. 2.28. From top to bottom: multi-columns reflectivity (panel a), average multi-columns reflectivity (panel b), single-column reflectivity (panel c), single-column total attenuation (panel d).

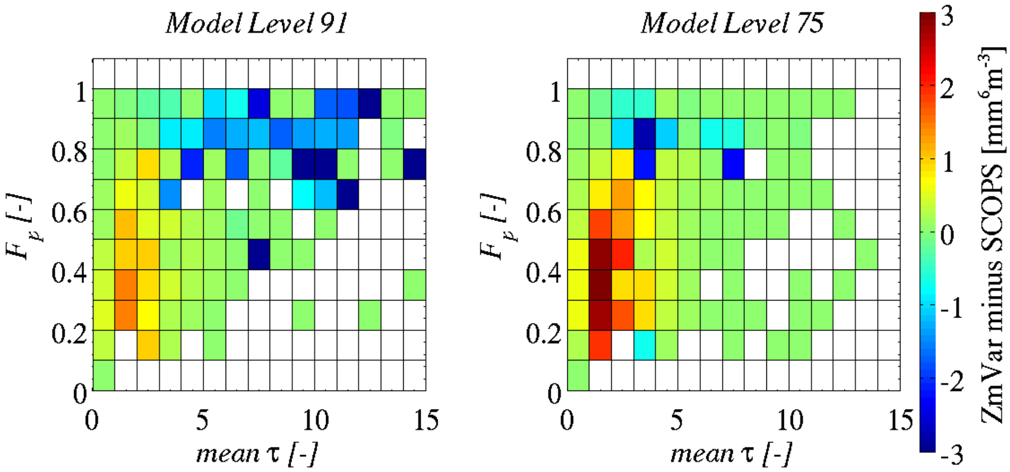

Figure 2.30: Mean difference between ZmVar simulated reflectivity in single-column and multi-column modes as function of precipitation fraction and total path attenuation. Left panel refers to model level 91 (closest to the surface) and right panel to model level 75 (about 800 hPa).

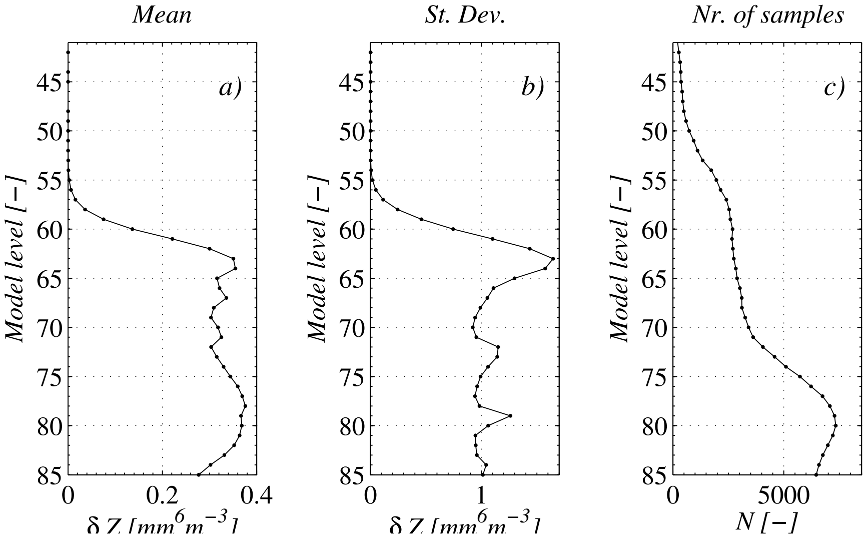

Figure 2.31: Difference between ZmVar simulated reflectivity in single-column and multi-column modes along model levels. Left panel contains the mean, central panel contains the standard deviation and the right panel the number of samples.

Nr. of subcolumns	***Time (sec)***	***Incr. difference (sec)***	***Difference (sec)***	***Difference (%)***
1	784	-	-	-
10	787	3	3	+0.4
20	810	23	26	+3.0
30	838	28	54	+7.0
50	867	57	83	+10.5

Table 2.1: Computational cost of ZmVar using different numbers of subcolumns.

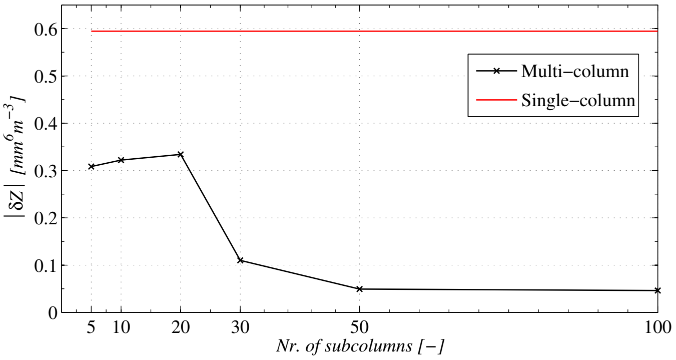

Figure 2.32: Absolute mean difference between reflectivity obtained using ZmVar with the number of columns in abscissa and a reference of 300 columns (black line). Red line indicates difference between the reflectivity obtained using ZmVar in single-column and the reference of 300 columns.

measured from the CloudSat radar (having a resolution of 1 km) falling within a model grid box were horizontally and vertically averaged to match the model resolution. Fig. 2.33 shows the difference between simulated Z^a and corresponding CloudSat measurements using the SC (black curve) and the MC (red curve). Mean reflectivity differences are plotted in Panel a). Zs simulated using the MC approach are always slightly closer to observations, except between model levels 63 and 70 ($\sim$470 hPa and $\sim$670 hPa, respectively).

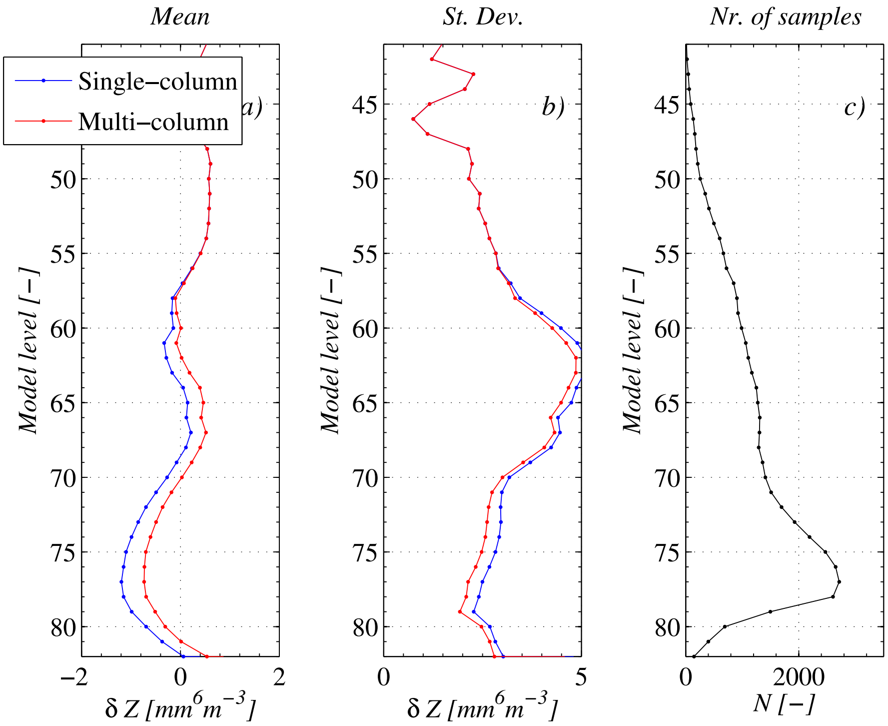

Figure 2.33: Difference between ZmVar simulated reflectivity in single-column and multi-column modes and co-located CloudSat observations along model levels. Black curves indicate ZmVar using single-column and red curves the multi-column method. Left panel contains the mean, central panel contains the standard deviation and the right panel the number of samples.

2.2.6 Precipitation fraction in ZmVar and SCOPS

Single-column and multi-column give different values of precipitation fraction. In case of MC the profile precipitation fraction can be defined as the mean (of zeros and ones) across all the sub-columns. As mentioned, for consistency, the comparisons described above were made replacing for the SC the original definition in Eq. 2.17 with the mean values obtained from the MC run. However, it is also interesting to investigate the differences between these values and to quantify the impact on Zs. Left panel of Fig. 2.34 shows the mean precipitation fraction profile evaluated on the same large dataset used. On average, the one of ZmVar gives significantly larger values close to the surface (0.75 vs. 0.55), although difference decreases going higher. Corresponding differences in Zs (ZmVar minus SCOPS) are shown in the right panel of Fig. 2.34, obtained running ZmVar in SC mode. ZmVar is lower below model level 65 and the difference increases as altitude decreases. This is compatible with the higher precipitation fraction, which can result in higher signal attenuation. Conversely, above model level 65, ZmVar is larger than SCOPS. This can again be related to the larger precipitation fraction, which at these levels leads to higher Zs since the attenuation is here usually negligible.

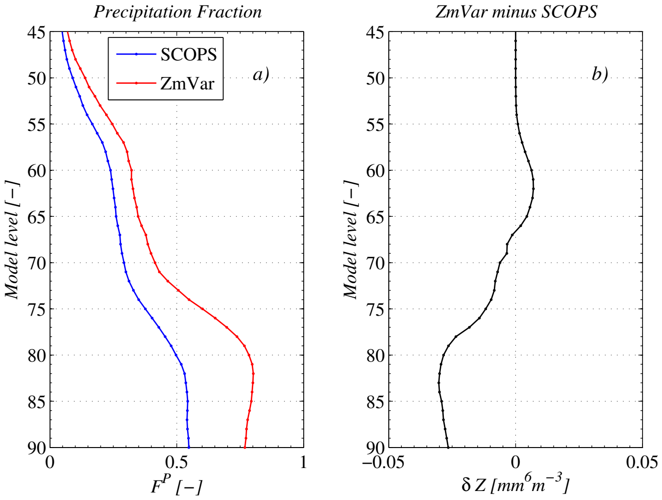

Figure 2.34: Panel a): Mean precipitation fraction defined by SCOPS (blue curve) and by ZmVar (red curve) evaluated on a large dataset of model profiles. Panel b): Differences between Z obtained using the ZmVar values and the ones from SCOPS. Calculations were made using the single-column mode.

2.2.7 *Sensitivity to cloud overlap scheme*

The maximum random formulation has been used in the previous tests as cloud overlap scheme being more realistic. It is worth however investigating what are the differences on Zs of changing cloud overlap scheme. Using the profiles in Fig. 2.28, ZmVar has been run in MC mode using 100 subcolumns and using the maximum-random, the random or the maximum as cloud overlap scheme. Fig. 2.35 shows the subcolumns generated for each profile in each of the three cases. Purple colour indicates bins where both rain and cloud are present; the orange colour represents bins with only precipitation, while cloudy-only bins are in blue. As expected, the highest number of subcolumns with some cloud or precipitation is produced for the case of random overlap (central panel), while the maximum overlap (bottom panel) produces the highest number of clear sky profiles. The maximum-random overlap case (top panel) looks similar to the random one, but with more overlap.

The decision of whether or not there is precipitation at each level depends on the presence of cloud in the layers above. As a consequence, the different overlap schemes have a different value for the mean precipitation fraction within the box. Fig. 2.36 shows that, with respect to the average precipitation fraction in the maximum-random case (top panel), the random assumption (central panel) leads to a quite substantial increase in precipitation fraction (ranging from 0.2 to 0.5). In the maximum overlap case (bottom panel), there is, as expected, a decrease of precipitation fraction, but less pronounced (never more than 0.2).

Figure 2.37 shows differences in the simulated Zs (attenuated) using different cloud-overlap schemes within SCOPS. Differences in the mean Zs generated are plotted in Panel b) and c) of the same figure. Panel b) shows that random overlap usually gives higher values than the maximum-random. Random overlap (top panel) represents the case with the lowest attenuation on the column. This translates in the highest values of attenuated Z also in the box. Another reason can be found in the fact that the number of cloudy sub-columns per box that the random overlap generates is larger. Therefore, similarly to what is described in Fig. 2.29, the attenuation within the box is lower. This effect is not related to the way layers overlap and, in fact, this is observed in regions with low attenuations, where the overlap scheme weakly influence the Z. The opposite occurs in cases where the attenuation above the layer is important: in this case (profiles 5 to 15) the maximum-random overlap produces heavy attenuation, while in the case of random overlap the signal keeps well above the minimum detectable signal. It can be shown that in these cases the maximum-random tends to generate more sub-columns with shallow but heavy precipitation profiles. These (few) cases have high Z because they are less affected by attenuation and therefore contribute to increase of the mean Z. Panels c) and d) show that the maximum overlap produces Z_a lower of both random and maximum-random because this case produces the smallest number of sub-columns with some cloud.

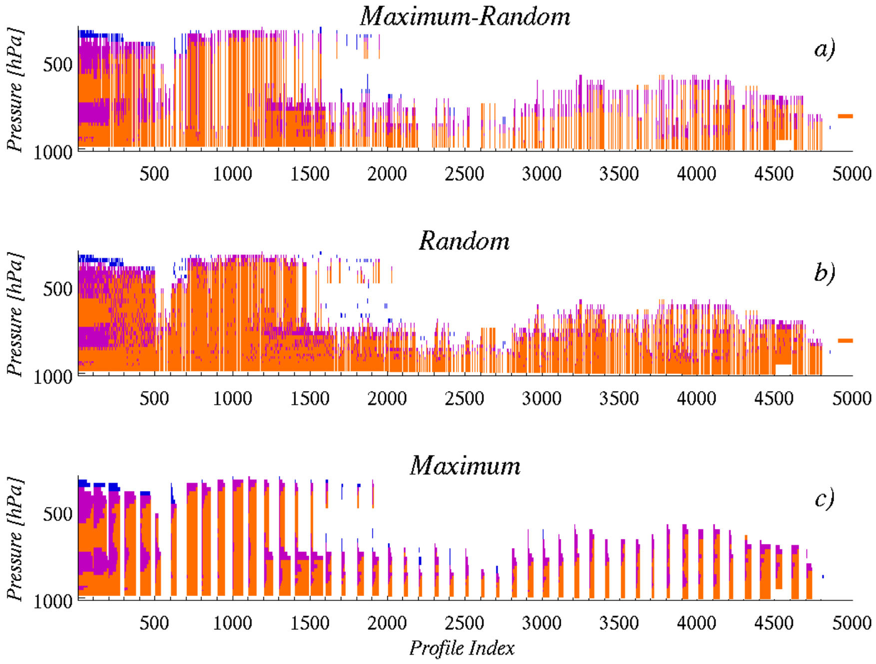

Figure 2.35: SCOPS overlap structure within grid box. Blue indicates that only cloud (liquid or ice) is present, orange only precipitation (rain or snow), and purple for both. From top to bottom: maximum-random, random, maximum overlap.

2.3 Conclusions

In order to use observations in NWP, a forward model is required to transform the model variables to the observed quantity. This section has described two forward models for radar reflectivity; the CFMIP Observation Simulator Package (COSP) radar simulator for CloudSat (Haynes *et al.*, 2007) and an ECMWF radar reflectivity model that has been used in the past for assimilation studies (Benedetti and Janisková 2004, Janisková 2004, Lopez *et al.* 2006) modified for use with CloudSat (ZmVar). The comparison has highlighted a number of issues related to the formulation of both radar reflectivity models and has been vital in assessing and improving the appropriate formulation for use within this project for both verification and data assimilation.

The forward operator is required to have an appropriate formulation for application to CloudSat data, the ECMWF model variables and the spatial resolution of the NWP model, but must also be computationally efficient. In addition, an assessment of the uncertainties in the forward model and the understanding of the sensitivities to these uncertainties (from both microphysics and sub-grid heterogeneity) is an important part of quantifying the error characteristics of the forward model. There are many uncertainties, but one of the largest sensitivities relates to uncertainties in the assumed particle size distributions (PSDs). Comparisons with *in situ* observations (e.g. Hong *et al.*, 2008) suggest the PSDs, at least for the frozen particles, are

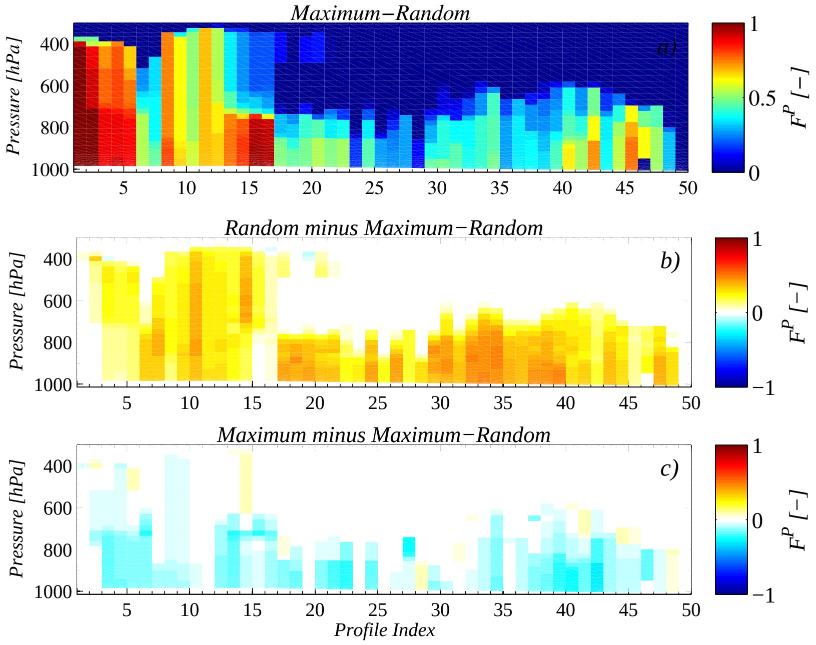

Figure 2.36: SCOPS precipitation fraction using different cloud-overlap schemes. Top panel: maximum-random, central panel: random minus maximum-random, bottom panel: maximum minus maximum random.

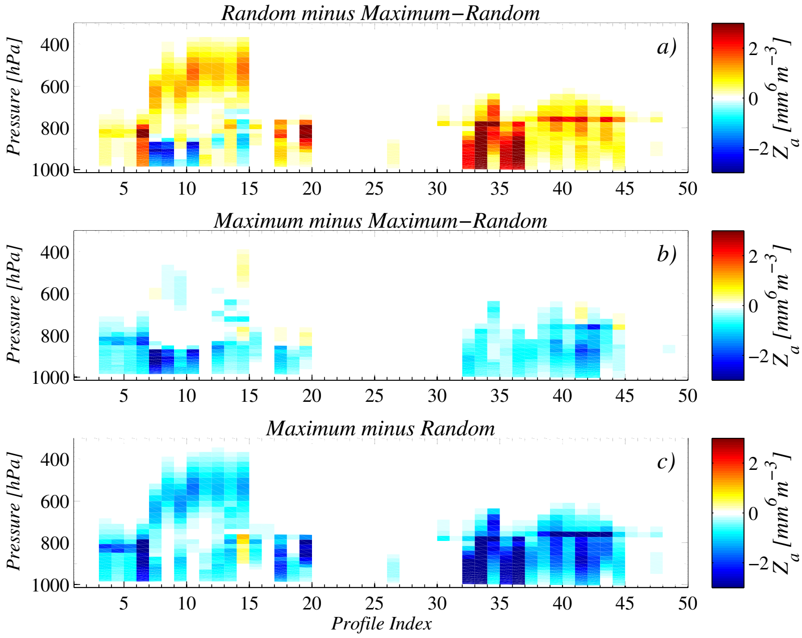

Figure 2.37: Differences in simulated Z using different cloud-overlap schemes within SCOPS. From top to bottom: random minus maximum-random, maximum minus maximum-random, and maximum minus random.

improved in the updated version of ZmVar. Further comparison with observed datasets will help to narrow down this uncertainty, but there will always be some error as hydrometeor PSDs vary considerably in space and time.

The NWP model contains various assumptions about sub-grid heterogeneity (cloud fraction, precipitation fraction, cloud overlap). Although the assumptions in the forward model should reflect those in the NWP model, it is instructive to assess the impact of different sub-grid assumptions on the modelled radar reflectivity profiles, and these are not always negligible. The sensitivity of the results to the use of a single-column or multi-column approach is generally smaller than for the uncertainties in PSDs, but can be significant under certain circumstances (e.g. where the signal is totally attenuated in the single column approach). The multi-column approach removes some of these differences, but is more complex to implement. A single column approach is adequate for data assimilation studies to avoid too much complexity for the adjoint model, but a multi-column approach is desirable for the verification studies where only the forward model is required.

In summary, a main outcome of work package 1000 is an improved radar reflectivity forward model (Zm-Var) for use in the assimilation and verification studies and an assessment of the main uncertainties and sensitivities that will help to define appropriate error characteristics during the assimilation studies.

3 Errors and biases related to the representativity problem

3.1 Introduction to the representativity problem

While CloudSat and CALIPSO observations offer an unprecedented vertical resolution of clouds and precipitation the horizontal coverage of these instruments is rather poor. Indeed, compared to the 2 dimensional extent of the surface of a model grid box, the horizontal information of these measurements can be regarded as quasi one dimensional. This makes a direct comparison with parameters computed by an NWP or climate model problematic, as estimating a 2D mean value by taking averages along a 1D line generally leads to both, systematic (i.e. biases) and random (variance) errors. A good estimate of these errors is crucial for model-observation comparisons as well as for data assimilation.

3.1.1 The representativity problem

While great discrepancies between model and measurement scales are less problematic for sufficiently smooth atmospheric fields, representativity issues are important for variables which exhibit strong spatial variations on the sub-grid scale as it is typical for cloud and moisture related fields. In data assimilation the error due to the representativity problem forms a part of the total observation error. The magnitude of the observation error determines the weight given to the observation in the assimilation process. If the assumed error is large this weight is small and so is the potential impact of the respective observation. An underestimation of the error, on the other hand, may have a detrimental impact on the assimilation process as the analysis is drawn closer to the observation than the quality (reliability) of the measured values justifies.

Due to its important role, a lot of effort has been devoted to derive an estimate for the representativity error (and bias) resulting from the small footprint of these measurements. More precisely, it was decided to derive a *flow dependent* error estimate as the magnitude of this error is strongly dependent on the respective weather type (this was already recognised by Miller *et al.*, 2007).

3.1.2 General methodology

As a fully statistical solution of the representativity problem is far beyond the scope of this project, priority was given to a more heuristic approach which includes the generation of synthetic data by stochastic modelling techniques. These techniques are widely used in Geostatistics (see Chiles and Delfiner, 1999, for an overview), e.g., for the exploration of natural resources, where direct measurements (or probes) are generally sparse but a good estimate of the underlying geophysical situation can be of huge economic importance.

In the current project a stochastic modelling technique is used in conjunction with a measure or score which can be computed from the data along the satellite track and which is used to differentiate regions into different groups for which the magnitude of the representativity error is different. More precisely, the approach taken (and described in more detail in the rest of this section) is comprised of the following steps:

1. Statistical considerations led to the choice of a measure (the “variogram maximum score”) which differentiates between situations with different confidence levels (i.e., different representativity error magnitudes). This statistical measure can be computed from the satellite track.

2. Statistical modelling techniques were employed (and further developed) to produce synthetic data that share some important statistical properties (marginal probability density function and spatial covariances) with the observations of interest.

3. Combining steps 1 and 2: Applying the variogram maximum score to the synthetic data, a quasi-empirical relationship was derived which links the score (measured along the satellite track) to the magnitude of the representativity errors.
4. The validity of the method was tested by using observations from scanning satellite instruments (MODIS and TRMM) for which the 2D truth is known.

3.2 Measuring flow dependency

The approach pursued in this project is to assess the representativity error from synthetic data generated with stochastic modelling techniques. One step of this approach is to relate regions from the satellite track to corresponding regions of the synthetic data. To facilitate this classification we use a measure (or "score") which can be computed from the satellite track and which differentiates between regions in which the magnitude of the representativity error is different. Finding a good score was crucial for the success of this project.

A simple flow dependent score is in principle readily obtained by the measured quantity itself. For example, when measuring cloud fraction at a certain grid scale length, the size of the representativity error will generally depend on the respective cloud fraction value computed within a given grid box. While this is a valid way of introducing some flow dependency for the representativity error, below, a more flexible measure is introduced which uses information not only from inside the grid box for which the cloud fraction or another variable is computed, but also from a larger region around this grid box. The new measure will be called "variogram maximum score" (or short "variogram score") as it is based on the variogram function.

3.2.1 The "variogram maximum score"

The score used in most of this work has been newly developed for this project and was named "variogram maximum score" (or short "variogram score") as it is based on the variogram (see Eq. 3.1 below for a definition). The variogram is a probabilistic measure which gives the decay of the covariance function along the satellite track. As we wanted to construct a *local* error estimate, variogram estimators have been computed locally, for different neighbourhoods centred around the points of interest (see Eq. 3.2). As the optimal size for this neighbourhood may itself be flow dependent, the maximum value over neighbourhoods of different lengths around the point of interest was taken as the actual measure. In this way the resulting measure is sensitive to information from different scales whereby the larger errors generally correspond to strong variations at smaller length scales (i.e., large variogram values in the smallest of the considered neighbourhoods).

For a random field $q(\vec{x})$ (where $\vec{x}$ is the location is space), the variogram $\gamma(\vec{x},\vec{h})$ (for a given displacement vector $\vec{h}$) can be defined as follows:

$$\gamma\left(\vec{x},\vec{h}\right) = 0.5\mathbb{E}\left\{\left[q\left(\vec{x}+\frac{\vec{h}}{2}\right)-q\left(\vec{x}-\frac{\vec{h}}{2}\right)\right]^2\right\} \tag{3.1}$$

where $\mathbb{E}\{..\}$ indicates the ensemble average. Note that for fields for which the statistical distributions are translational invariant (i.e., $\gamma\left(\vec{x},\vec{h}\right)=\gamma\left(\vec{h}\right)$ is independent of $\vec{x}$) one has $\gamma\left(\vec{h}\right)=C(0)-C\left(\vec{h}\right)$ where $C\left(\vec{h}\right)$ is the covariance function.

From the satellite track we construct a local estimator $\gamma(x_0,h,L)$ for $\gamma(\vec{h})$

$$\gamma(x_0,h,L) = 0.5\left\langle\left[q\left(x+\frac{h}{2}\right)-q\left(x-\frac{h}{2}\right)\right]^2\right\rangle_{x\in I[x_0,L]} \tag{3.2}$$

by taking the spatial average $\langle..\rangle_{x\in I[x_0,L]}$ over the neighbourhood $I[x_0,L] = [(x_0 - L),(x_0 + L)]$ of size $2L$ around x_0 (x_0 corresponds to the horizontal position of the centre point of the intersect between the satellite track and the model grid box of interest). The corresponding measure γ gives information about the variability at each point x_0. It depends on two length scale h and L. The displacement length h was chosen to be half the length of a grid box . Tests with different h seemed to indicate that the method is not very sensitive to the particular choice of this parameter.

To construct an error discriminator which comprises information from a larger range of scales, the variogram estimate Eq.(3.2) was computed for different neighbourhoods $I[x_0,L]$ (i.e. for different values of L, compare Fig. 3.1) and then the maximum of all the obtained values was taken. More precisely, neighbourhoods

$$L = kL_0\, with\, k \in \{1,2,..N_{max}\}$$

have been considered, where L_0 is the length of the NWP grid box and and N_{max} is the maximal number of considered grid boxes. Using this, the “variogram maximum score” $sc(x_0,h,L_0)$ has been defined as

$$sc(x_0,h,L_0) = max\left[\gamma(x_0,h,(k+0.5)L_0),k \in \{1,2,..N_{max}\}\right] \tag{3.3}$$

which turned out to be not too sensitive with respect to N_{max} as long as this number was large enough ($N_{max} = 10$ has been chosen). It should be noted that large score values are usually obtained only from the smaller neighbourhoods (small values of k) while contributions from larger ks are usually small (they only become relevant in Eq. 3.3 if the contributions from smaller neighbourhoods happen to be small). This reflects the fact that strong variations closer to a grid box have a larger impact on the representativity error (in a probabilistic sense) than perturbations which are further away.

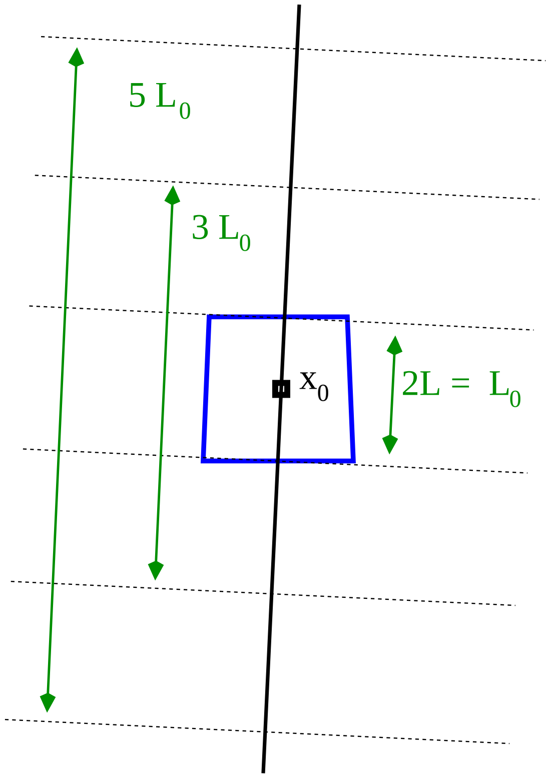

Figure 3.1: Horizontal projection of the satellite track (black bold line) intersecting a grid box.

3.3 Stochastic modelling

The stochastic modelling method used in this work generates synthetic data which have (almost) the same marginal probability density function (PDF) and the same covariance function as the satellite observations. It is assumed that the statistical properties are isotropic.

For Gaussian variables there are different methods to construct synthetic data with a prescribed covariance function (see Chapter 7 of Chiles and Delfiner, 1999). Of course, most variables are not normally distributed. As explained in more detail below, the procedure employed here for generating synthetic data consists of several steps whereby a major part is to project non-Gaussian observations onto a Gaussian field which is then modelled with one of the standard methods.

3.3.1 Modelling Gaussian fields

The method employed here for modelling a Gaussian field with a prescribed correlation function was taken from Pardo-Iguzquiza and Chica-Olmo (1993) and Pardo-Igúzquiza and Chica-Olmo (1994). It is a spectral method which generates the Fourier coefficients of the field. More precisely, the method uses the fact that the Fourier transform of a covariance function is the power spectrum, which constrains the Fourier coefficients and leaves only their complex phase to be determined. For Gaussian random functions the complex phase is homogeneously distributed and can therefore easily be computed by a random number generator.

An important condition for generating synthetic data is that the employed covariance function is reasonably smooth. It should be kept in mind that covariances “measured” from observations are always a statistical estimate and, particularly for longer distances, the convergence of this estimate can be problematic. While the power spectrum from true covariance functions is always positive definite, this property is generally not true for estimated covariances. As positive definite power spectra are essential, for generating the synthetic data, the covariances obtained from observations are replaced by a smooth analytic function fitted to the observed covariances.

At large distances, it is crucial for the method employed, that the chosen covariance function decreases smoothly to zero and that the model domain (i.e., the domain for which synthetic data are produced) is chosen to be large compared to the decay rate. For data for which correlations decrease very slowly this may pose a dilemma as large domain sizes make simulations very time consuming. As the representativity error is most likely dominated by the short-range behaviour (unless for extremely large NWP grid box sizes), generally, no effort was made to represent the large-scale behaviour very accurately (often this is not possible as the measured covariances are dominated by noise in this regime). Therefore, the analytic function mentioned above, which was fitted to the observed covariances, was optimised to fit *only the short-range behaviour* of the measured covariances and the decay rate at larger distances was taken from the short-range fitting region.

3.3.2 Variable transformations for non-Gaussian variables

As general observational data are not normally distributed, a transformation is needed which “projects” the satellite data onto Gaussian fields.

Continuous variables

If the field of interest is continuous such a transformation is, in principle, straight forward and the employed method to generate synthetic data takes the following steps:

1. Computing the probability distribution function $F_{ob}\left(q_{ob}\right)$ for the observations q_{ob}.
2. Using $F_{ob}\left(q_{ob}\right)$ to construct a transformation (called the forward transform)
$$q_{ga} = q_{ga}\left(q_{ob}\right) \tag{3.4}$$
which relates the observations q_{ob} to a field q_{ga} which is normally distributed (with variance 1).
3. Using Eq. 3.4 to transform the observed field $q_{ob}\left(\vec{x}\right)$ and then computing the spatial covariances from the transformed data $q_{ga}\left(q_{ob}\left(\vec{x}\right)\right)$.
4. Using stochastic modelling techniques to generate a Gaussian field which has the spatial covariances computed in step 3.
5. Inverting Eq. 3.4 to obtain a relation (called the back transform)
$$q_{ob} = q_{ob}\left(q_{ga}\right) \tag{3.5}$$
which is then used to transform the modelled Gaussian field into observation space.

For a continuous variable the forward transform (Eq. 3.4) is given by

$$q_{ga}\left(q_{ob}\right) = F_{ga}^{-1}\left[F_{ob}\left(q_{ob}\right)\right] \tag{3.6}$$

where $F_{ob}\left(q_{ob}\right)$ is the distribution function (i.e., the integral of the PDF) of the observations while F_{ga} is the corresponding distribution function of a Gaussian field. If the observed values are continuous, Eq.(3.6) can be inverted which yields the back transform:

$$q_{ob}\left(q_{ga}\right) = F_{ob}^{-1}\left[F_{ga}\left(q_{ga}\right)\right] . \tag{3.7}$$

Representing discrete variables

For discrete variables $q_{ob} \in \left\{q_{ob}^{(k)}\right\}$ with $(k = 1, 2, ..N_{max})$ transformations 3.6 and 3.7 are only defined for discrete values $q_{ob}^{(k)}$ and $q_{ga}^{(k)}$ with

$$\begin{aligned} q_{ga}^{(k)} &= q_{ga}\left(q_{ob}^{(k)}\right) \\ &= F_{ga}^{-1}\left[F_{ob}\left(q_{ob}^{(k)}\right)\right] \end{aligned}$$

(with $q_{ga}^{(N_{max})} = \infty$). If the discrete levels are sufficiently close, a Gaussian distribution is still a good approximation so that the variable can be treated as quasi continuous. In the more general case, however, i.e. for variables with more isolated discrete levels, the discrete variable $q_{ga}^{(k)}$ produced by the forward transform 3.6 can become strongly non-Gaussian.

Also in the discrete case, however, the non-Gaussian discrete variable is, in principle, embedded in a continuous Gaussian variable q_{ga}. The idea is to represent the discrete observations $q_{ob}^{(k)}$ through this continuous field q_{ga} which can be generated by the stochastic modelling technique (provided one knows the correct correlation function for q_{ga} whose derivation will be discussed further below). To represent the discrete observations $q_{ob}^{(k)}$ by a continuous Gaussian variable q_{ga} we assign all values of q_{ga} in the interval

$q_{ga}^{(k-1)} < q_{ga} \leq q_{ga}^{(k)}$ to $q_{ob}^{(k)}$ (where for the case $k = 1$ the definition $q_{ga}^{(0)} = -\infty$ has to be used while $q_{ga}^{(N_{max})} = \infty$ as mentioned above). Doing this we generalise Eq. 3.7 through

$$q_{ob}\left(q_{ga}\right) \quad = \quad q_{ob}^{(k_m)} \quad \text{with } q_{ga}^{(k-1)} < q_{ga} \leq q_{ga}^{(k)} \tag{3.8}$$

which ensures that the probability p_{ob}^{k} of the discrete value $q_{ob}^{(k)}$ is the same as the probability that q_{ga} is in the interval $\left[q_{ga}^{(k-1)}, q_{ga}^{(k)}\right]$. More generally one has

$$\int\limits_{-\infty}^{q_{ga}^{(k)}} P_{ga}\left(q_{ga}\right) q_{ob}\left(q_{ga}\right) dq_{ga} \quad = \quad \sum_{l=0}^{k} p_{ob}^{l} q_{ob}^{(l)} \tag{3.9}$$

where $P_{ga}\left(..\right)$ is the Gaussian probability density function (PDF).

The problem, however, is to find the correlation function which q_{ga} has to have in order that the covariance function of $q_{ob}^{(k)}$ corresponds to the observations. Since the field $q_{ga}^{(k)}$ generated by the forward transformation Eq. 3.6 is not normally distributed, step 3 above does not give the correct covariance. In other words, a Gaussian field with this covariance does not produce (when transformed back) synthetic data which have the same covariance function as the observations. This problem led to the development of the other methods described below.

Transforming covariances for binary variables

An extreme case of a discrete field is a binary field q_{bi} which can be represented by a Gaussian field together with a threshold value θ:

$$q_{bi}\left(q_{ga}\right) \quad = \quad \begin{cases} 1 & q_{ga} \geq \theta \\ 0 & q_{ga} < \theta \end{cases} . \tag{3.10}$$

Here the value of θ is readily obtained from the condition that the global mean $\overline{q_{bi}\left(q_{ga}\right)}$ of $q_{bi}\left(q_{ga}\right)$ has to be the same as for the observations. The covariances of the Gaussian field can be found by (numerically) inverting the relation $\hat{\sigma}\left(\sigma\right)$, where $\sigma \equiv \mathbb{E}\left\{q_{ga1} q_{ga2}\right\}$ is the correlation of values from the Gaussian field taken at different locations ($q_{ga1} = q_{ga}\left(x_1\right)$ and $q_{ga2} = q_{ga}\left(x_2\right)$) and $\hat{\sigma} \equiv \mathbb{E}\left\{q_{bi}\left(q_{ga1}\right) q_{bi}\left(q_{ga2}\right)\right\}$ is an expectation value which can be obtained from the observations. The relation $\hat{\sigma}\left(\sigma\right)$ can be obtained from the general formula for the joint probability of two correlated Gaussian fields

$$P\left[\sigma\right]\left(u,v\right) \quad = \quad \frac{1}{2\pi\sqrt{1-\sigma^2}} \mathbf{exp}\left[-\frac{u^2+v^2-2\sigma uv}{2\left(1-\sigma^2\right)}\right] \tag{3.11}$$

where u and v are two correlated Gaussian fields (with zero mean and variance one) and $\sigma \equiv \mathbb{E}\left\{uv\right\}$ is their correlation. Using this the expectation value of $\hat{\sigma} \equiv \mathbb{E}\left\{q_{bi}\left(q_{ga1}\right) q_{bi}\left(q_{ga2}\right)\right\}$ is given as

$$\hat{\sigma}\left(\sigma\right) \quad = \int_{-\infty}^{\theta} \int_{-\infty}^{\theta} \quad P\left[\sigma\right]\left(q_{ga1}, q_{ga2}\right) dq_{ga1} dq_{ga2} \tag{3.12}$$

This equation can then be (numerically) inverted to obtain the desired transformation $\sigma = \sigma\left(\hat{\sigma}\right)$, between the product $\hat{\sigma} \equiv \mathbb{E}\left\{q_{bi}\left(x\right) q_{bi}\left(x+h\right)\right\}$ and the corresponding covariance σ of the Gaussian field (the transformation has to be applied for each value of h independently).

Generalisation to discrete and mixed variables

For modelling such type of data as the MODIS $5km$ cloud fraction product the standard methods described above had to be extended. The cloud fraction values were (apparently) produced by the averaging over 5x5 binary fields. The PDF has 26 discrete levels $C_{frac} \in \{k * 1/25\}$ with $k \in \{0,1,2,..,25\}$. 24 of these levels (those with $0 < C_{frac} < 1$) were close enough together to be treated as being continuous. Roughly 40% of the levels had $C_{frac} = 1$ and around 20% had $C_{frac} = 0$. The challenge was to find a method which combines the quasi-continuous with the discrete part.

As explained above, computing the covariance function of the discrete field by transforming the observed values with Eq.(3.6) is not a valid option since the forward transformed observations are not normally distributed. Instead, point 3 above has been replaced by several sub steps which use Eq.(3.11) in combination with definition (3.8) to obtain the relationship for the expectation value $\hat{\sigma} = \hat{\sigma}(\sigma)$:

$$\hat{\sigma}(\sigma) \quad = \int_{-\infty}^{+\infty} \int_{-\infty}^{+\infty} \quad P[\sigma](q_{ga1}, q_{ga2})\, q_{ob}(q_{ga1})\, q_{ob}(q_{ga2})\, dq_{ga1} dq_{ga2}\,. \tag{3.13}$$

Again, as for the binary case discussed above, this equation can then be (numerically) inverted to yield the correlation for q_{ga} as a function of the expectation value $\hat{\sigma} \equiv \mathbb{E}\{q_{ob}(x)\, q_{ob}(x+h)\}$.

The general method

Using Eq. 3.13 for deriving the covariances, points 1-5 above, which described the general method for modelling continuous fields can now be generalised to discrete and mixed fields as follows:

1. Computing the probability distribution function $F_{ob}(q_{ob})$ for the observations q_{ob}.
2. Using $F_{ob}(q_{ob})$ to construct the forward transform.
3. a) Using Eq.3.13 to compute $\hat{\sigma}(\sigma)$.
   b) Computing the product $\hat{\sigma}(h) \equiv \mathbb{E}\{q_{ob}(x)\, q_{ob}(x+h)\}$ from the observations.
   c) Inverting (numerically) the relation $\hat{\sigma}(\sigma)$ to obtain the correlation function
   $\sigma(\hat{\sigma}(h)) = \mathbb{E}\{q_{ga}(x)\, q_{ga}(x+h)\}$ of the Gaussian field.
4. Using stochastic modelling techniques to generate a Gaussian field which has the spatial covariances computed in step 3.
5. Using Eq. 3.8 to transform the modelled Gaussian field into observation space.

To demonstrate the usefulness of this method, it will be applied to different types of observations in the next subsection.

3.4 Testing with observations

The statistical treatment which was outlined in the last subsection is not a mathematically rigorous method. As explained above, the synthetic data which it creates share, within some approximation, important statistical properties with the observed data. To which extent this leads to a sufficient estimate of the representativity error had to be tested. This subsection describes the tests and their results. The positive outcome of these tests would give us some confidence for applying the method to CALIPSO and CloudSat data for which the true representativity error is not known.

3.4.1 Modelling the test data

The validity of the proposed method has been tested with 3 types of observed data. As these test data are coming from a scanning satellite instrument, a direct comparison between 1D segments and 2D area averages is possible. The following data have been selected:

- MODIS total cloud cover (5 km product)
- TRMM rain index (i.e. fraction)
- TRMM rain rate

For the purpose of this study, 5 days of data have been analysed. Data has been taken from a region in the tropical Pacific (longitude$\in [155 - 256]$, latitude$\in [20S - 20N]$).

Figure 3.2 shows the distribution function of the TRMM rain rates for observed (red curve) and modelled (black curve) data. By far the largest peak is in the zero rain-rate bin (i.e., no rain) which is for more than 96.5 % of the cases (96.51% for the observed, 96.52% for the modelled data). The number of occurrences decreases very rapidly with increasing rain rate. The largest observed values were around 260 mm/h for the observation period. Events with rain rates much larger than 100 mm/h were, however, relatively rare.

Figure 3.3 (bottom) shows the corresponding distribution for the MODIS cloud fraction (C_f) data. The employed 5km product apparently stems from averaging over 25 (i.e., 5x5) binary points so that data are distributed over 26 discrete levels. The largest sample fractions are in the $C_f = 1$ (38.3% observed, 37.9% modelled) and $C_f = 0$ (18.6% observed, 19.6% modelled) bins. The top graph of Figure 3.3 shows the corresponding 25 threshold values $q_{ga}^{(k)}$ (note that $q_{ga}^{(26)} = \infty$) which were used for the back transformation Eq. 3.8.

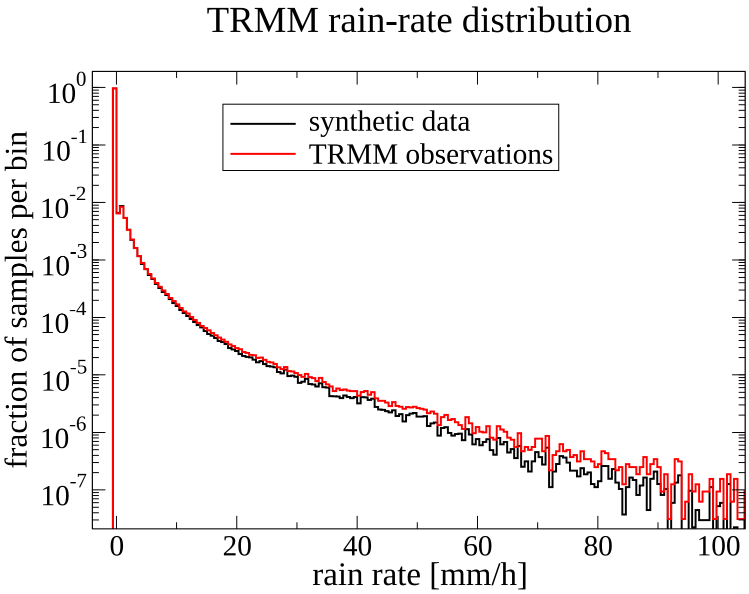

Figure 3.2: Distribution of rain rates in observed (red curve) and synthetic (black curve) TRMM data. The left outer bin (which is plotted against an interval of negative rain rates) corresponds to points with no rain (zero rain rate) for which a separate bin has been assigned.

Figure 3.4, graphs a-c, show the covariance functions obtained from the observations (green curves) and the corresponding synthetic data (black curves). For the TRMM data, synthetic rain fractions and rain rates are

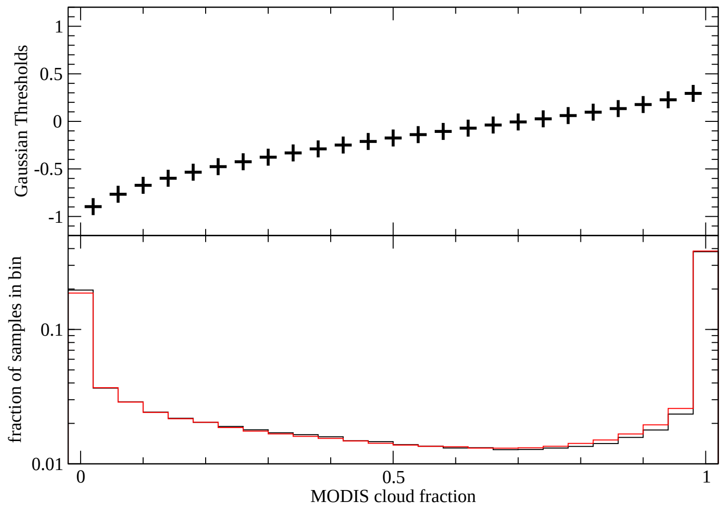

Figure 3.3: Bottom: Distribution of cloud fraction for the observed (red curve) and synthetic (black curve) MODIS data. Top: The corresponding thresholds for back transforming the Gaussian field.

both obtained from the same Gaussian field. This field was optimised to fit the index (or rain fraction) field. It is therefore not surprising that the fit between observed and synthetic covariance function is much better for the rain fraction than for rain rates. It will, however, be shown below that the synthetic rain rate field also yields reasonable estimates for the representativity error of this field.

Generally, no effort was made for the covariance functions of the synthetic data to fit the long distance behaviour of the observed covariances. For TRMM data, covariances at distances larger than 300 measurements points (from the TRMM radar) are clearly dominated by noise (i.e. insufficient convergence). For MODIS (black curve in Figure 3.4 c) the long distance behaviour is smooth but non-monotonic (with a strong minimum around 2000 km). As the representativity error is most likely dominated by the short-range behaviour (unless for extremely large NWP grid box sizes) no effort was made to represent this non-monotonic behaviour with the synthetic data.

The correlation function for the MODIS data together with the correlation function of the corresponding Gaussian generating field (obtained by inverting Eq. 3.13) are plotted in Figure 3.4 d (black and blue curves). As explained above, the synthetic data for the Gaussian field were generated using an analytical fit to the covariance estimated from the observations. This analytical fit is given by the red curve in Fig. 3.4d.

3.4.2 Results

To determine the representativity error averages of different quantities (e.g., cloud fraction) have been computed on (1D) line segments as well as for the corresponding (2D) grid boxes which contain the respective line segments. The line segments have been partitioned into bins of the respective score (for most of the results presented below the "variogram score" has been used, see subsection 3.2) and the root mean square (rms) error has been computed as the rms difference between line and grid box averages in each bin, respectively.

From the Fig. 3.5a) one finds that the employed variogram score $sc(x_0, h, L_0)$ (see Eq. (3.3), here $L_0 = 65$ and $h = 35$ had been chosen) is quite effective in differentiating between regions with small and large errors. More precisely, strong differences are found in the sc interval $[0, 0.2]$ while only small changes occur for

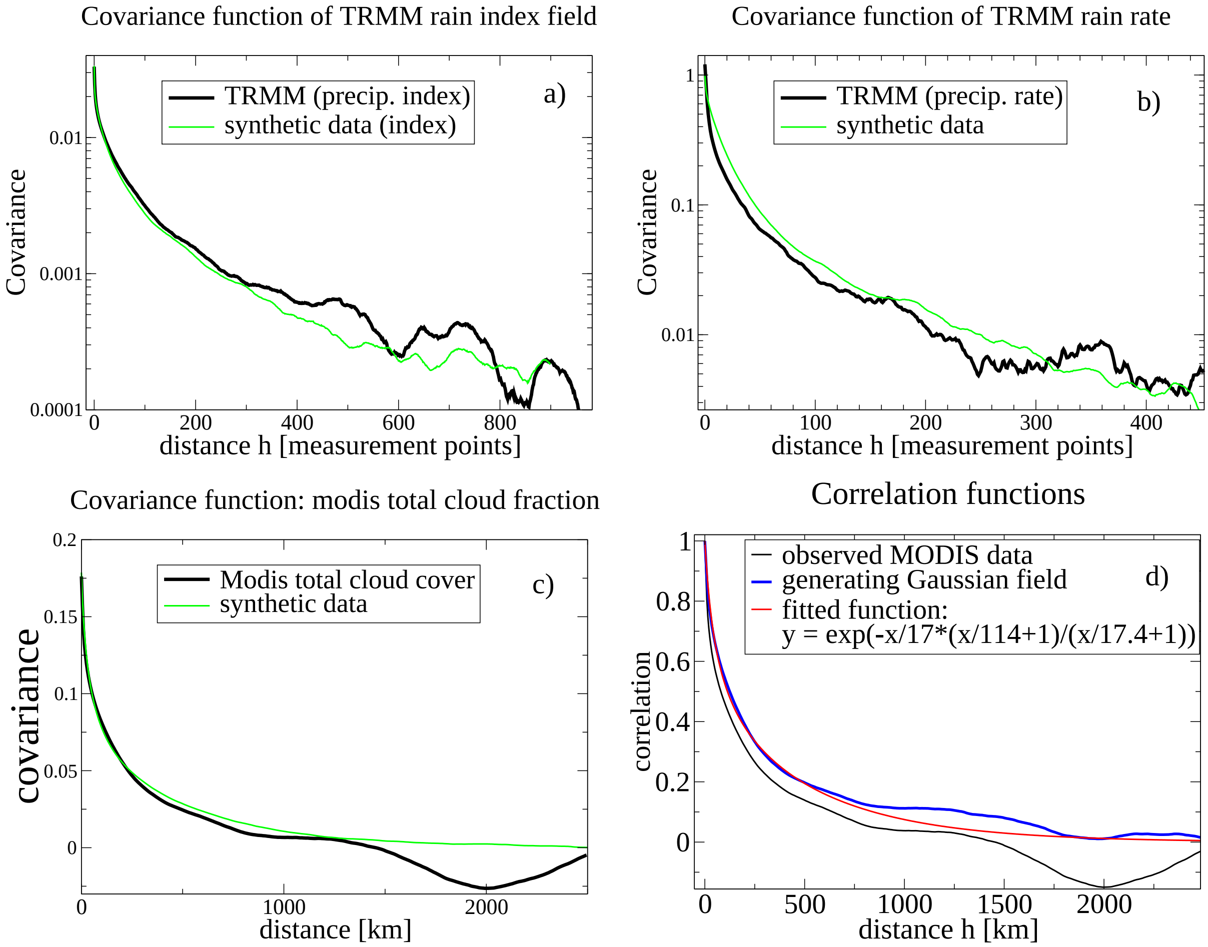

Figure 3.4: Graphs a)-c): Covariance functions for the observed data (black curves) with the corresponding functions obtained from the synthetic data (green curves). Graph d) shows the correlation function for the observed MODIS data (black curve), the corresponding values of the generating Gaussian field (blue curve, compare text) and the fitted function (red curve) which was used to generate the synthetic data for the MODIS observations.

larger values of sc. As seen from Fig. 3.5b), a large part of the observed samples occur in the range of small sc for which the score differentiates well, while numbers decrease dramatically for $sc > 0.4$ for which the statistics become quite noisy.

Very encouraging is the excellent agreement between the rms errors obtained from observed and modelled values. While there is a large relative error in the $sc = 0$ bin (the error obtained from modelled data has about twice the magnitude of those from observations) differences are very small in absolute terms and the strong rms error increase in the interval $[0, 0.2]$ is captured quite perfectly by the modelled data.

The peak of the number distribution is generally captured quite well, though the observed peak is a little broader. Very significant differences between the number distributions are in the two smallest sc bins for which the observed data have a local maximum while for the synthetic data numbers decrease monotonically (with a strong minimum at $sc = 0$). This shows that the modelled data do not contain all the features of the cloud field. The observed field apparently has strongly uniform regions (which have either cloud fractions $cfr = 1$ or $cfr = 0$, respectively) which are not represented by the modelled data. Nevertheless the modelled data capture the error dependence on sc quite well.

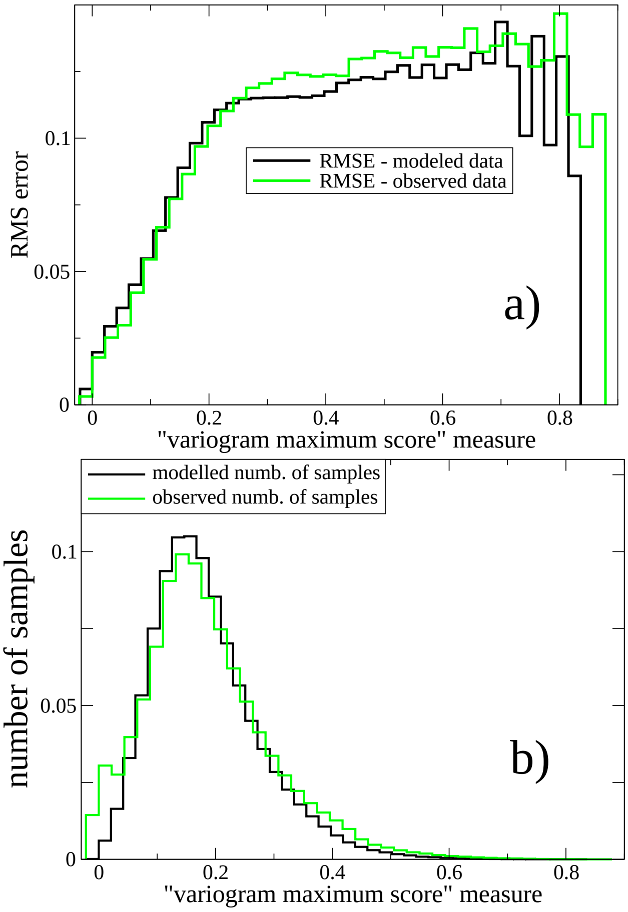

Figure 3.5: From MODIS data: Root mean square error (RMS error, graph a) and number concentration (graph b) for bins corresponding to different intervals of the variogram maximum score sc (see Eq. 3.3) as indicated by the respective lower axis. The most left bin (with $sc \leqslant 0$) corresponds to regions with $sc = 0$ for which a separate bin has been selected. Green lines are from observations, black lines correspond to the same quantity but computed from modelled (i.e., synthetic) data.
The RMS errors were computed as the difference between the cloud fraction value taken from a 2D square area (65 km x 65 km) and a cloud fraction estimate taken from a 1D segment of 65 km length (the 1D segments were taken from a centre line of the 2D squares).

For TRMM precipitation fraction, the corresponding error dependencies are given by the bold curves in Fig. 3.6. While the agreement between observed and stochastically estimated error values is excellent for small sc ($sc < 0.2$), for larger values the errors obtained from observations are up to 20% larger than those from synthetic data. While this results are a little less accurate than those found for MODIS data, a 20% deviation should still be completely acceptable for most meteorological applications.

Deviations of the same magnitude can be seen in Fig. 3.7 (left graph) for the TRMM rain rates. Only for $sc = 0$ the observations differ from the modelled error value by more than a factor 2 (as the modelled value for $sc = 0$ is extremely small; however, the difference between modelled and observed errors is still small in absolute terms).

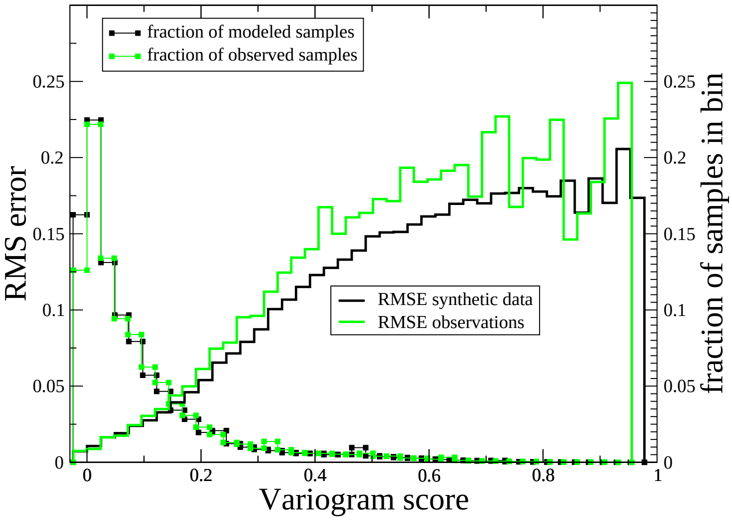

Figure 3.6: Similar to Fig. 3.5 but for rain fractions from TRMM data. The length of the 2D square and 1D segments are 22 radar shots. Bold lines show RMS errors and thin lines with square symbols the corresponding number concentrations. Green lines are from observed, black lines from synthetic data.

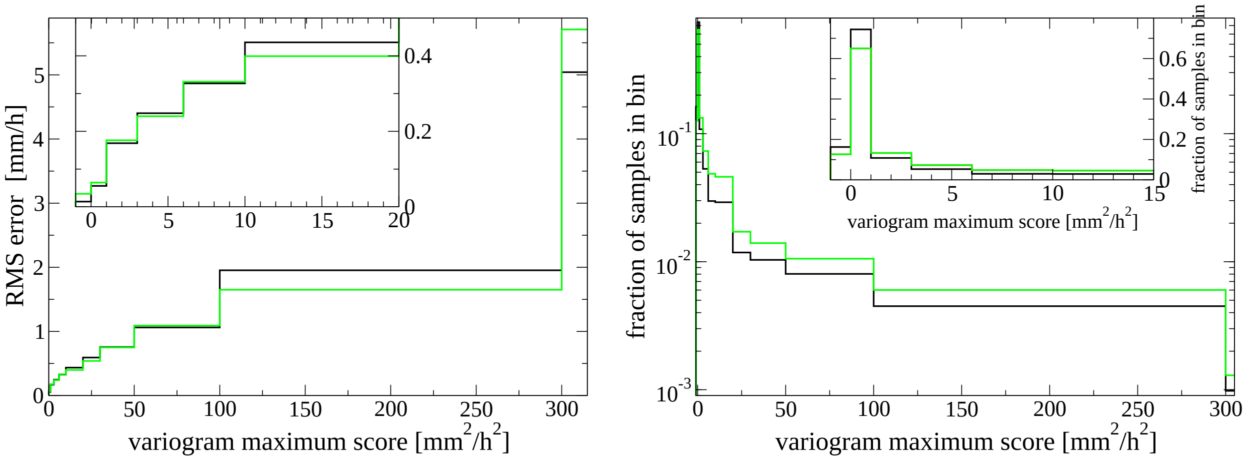

Figure 3.7: Similar to Fig. 3.6 for TRMM rain fraction but for rain rate. The left graph shows the RMS error (RMS difference between 1D and 2D rain rate estimates or measurements) while fraction of samples are shown on the right. As in Figs. 3.6 and 3.5, all quantities are computed for bins corresponding to intervals of the variogram score. The inlets magnify results for small variogram score values.

Biases and variance

For meteorological applications it is useful to partition the total RMS errors shown in Figs. 3.5, 3.6 and 3.7 into bias and variance. While for the MODIS data the bias in a given *sc* interval is very small (see Fig. 3.8), substantial biases can be seen in Figs. 3.9 and 3.10 for TRMM rain fractions and rain rates. Again, values obtained from modelled and observed data mostly seem to agree within 20%. Big relative differences are found for the rain rate bias at comparably small values of *sc* ($sc \in [3,30]$). However, in this *sc* range biases are generally small and can be neglected.

For the corresponding variances (see right graphs of Figs. 3.9 and 3.10) differences between results from synthetic and observed data are of the same magnitude as found for the corresponding RMS errors (compare Figs. 3.6 and 3.7).

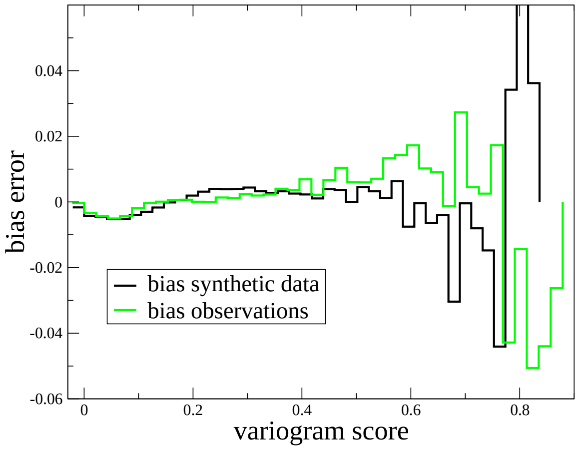

Figure 3.8: Biases for MODIS cloud fraction. Green lines correspond to observations while black lines are derived from synthetic data. As in Figs. 3.5 and 3.6, the bin plotted at negative sc values corresponds to $sc = 0$.

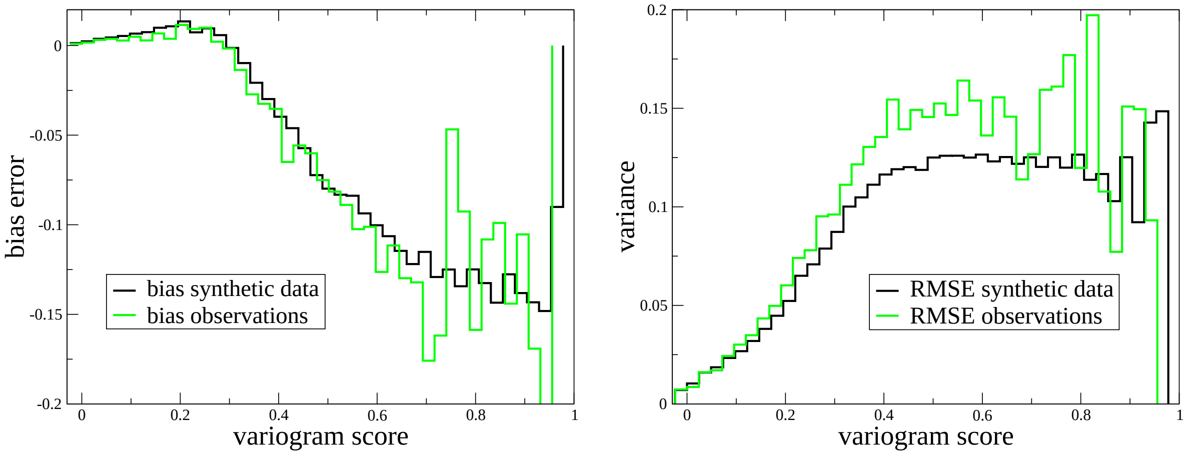

Figure 3.9: Biases and variance in variogram-score bins for TRMM rain fraction. Green lines correspond to observations while black lines are derived from synthetic data. As in Figs. 3.5 and 3.6, the bin plotted at negative sc values corresponds to $sc = 0$.

Scale dependency of the representativity error

In most of this section MODIS data are analysed with respect to 65km x 65km grid boxes. Of course, for different applications NWP and general circulation models (GCMs) are run with quite different resolutions. The operational resolution of the ECMWF deterministic forecast is about 24 km while the first inner loops of the 4D-Var system are run with grid boxes of about 200 km. This raises the question how the representativity error characteristics of the observed and stochastically generated data differ for different grid box sizes.

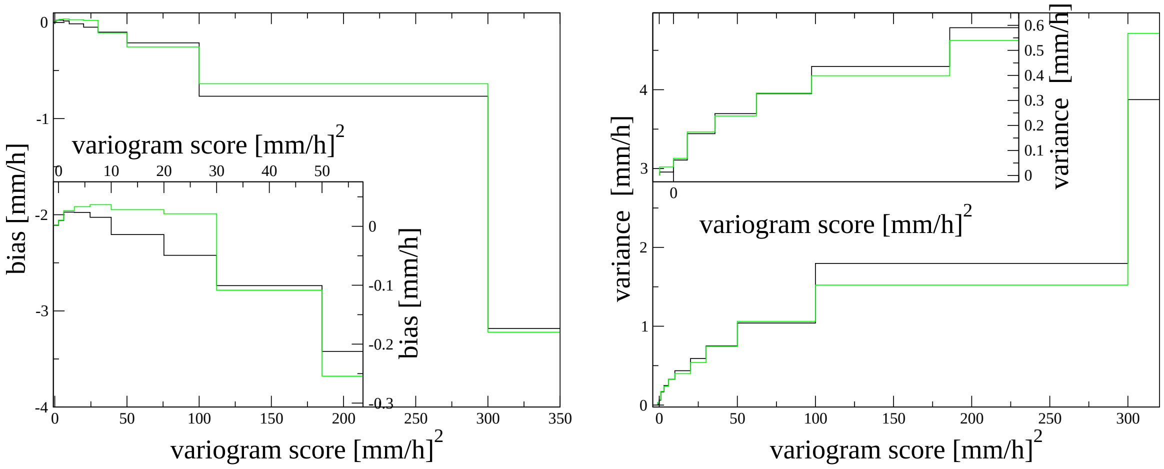

Figure 3.10: As Figure 3.9 but for rain rate.

To address this, representativity errors for MODIS data have been computed for several gridbox sizes. As seen in Fig. 3.11, the shape of the relationship between the variogram score *sc* and the RMS error varies only slowly with grid box length. However, the correspondence between the RMS errors computed from observations and synthetic data decreases with increasing grid box length scales. Most strikingly, for the largest considered gridbox sizes (225 km and 445 km), error estimates from synthetic data are only available above a certain threshold of the variogram score as the stochastically generated data have no samples in the smallest *sc* bins (compare Fig. 3.12). Also, near their onset (where, for small *sc*, RMS error estimates from synthetic data become first available) synthetic error estimates differ strongly from the observed errors (the estimates exhibit a large peak). This difference near the onset is not surprising as sample sizes are still comparably small.

These results suggest that the proposed stochastic method for estimating the representativity error will perform best for smaller grid box sizes while the methods reliability decreases with increasing grid box size. When applying the method to CloudSat and CALIPSO data, it will be important to assess for which scales the method can be trusted. Encouraging in this context is the fact that for the tests presented here, parameter regimes where the method becomes unreliable coincide with those where the sample number distributions (see Fig. 3.12) differ strongly between observed and synthetic data. It is therefore likely that failures of the method can be diagnosed by comparing the correspondence between statistics of the two data sets along the satellite track.

Using cloud cover and rain rates or fractions as score

So far this part of the report has concentrated on the newly developed variogram score which was found to be a useful tool for differentiating regions with different error magnitudes. As mentioned above, a very simple measure for the flow dependence of the representativity error is usually obtained by the measured quantity itself. For comparison Figure 3.13 shows the RMS error for TRMM radar rain fraction as a function of the rain fraction itself. Differences between results from modelled and observed data seem to be of comparable magnitude (possibly slightly larger in some cases) as for the variogram score (compare Fig. 3.6). The same seems to be true for the biases and variances shown in Figure 3.14 (compare Fig. 3.9).

Results for the TRMM radar rain rate shown in Figs. 3.15 and 3.16 show also good agreement apart from

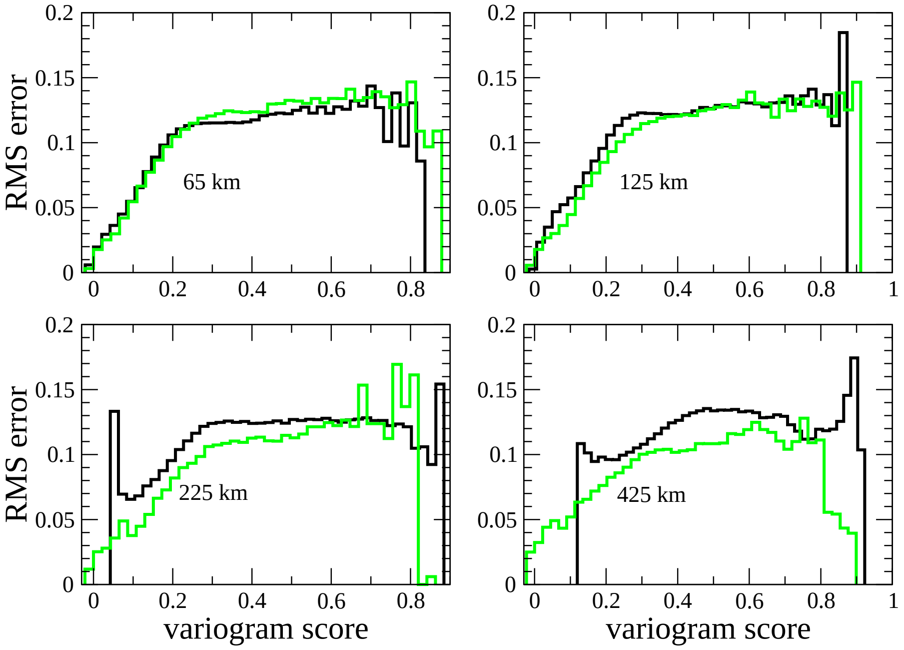

Figure 3.11: Results for grid boxes of different sizes for RMS errors of observed MODIS data (green lines) and the corresponding synthetic data (black lines). As indicated in each graph, different graphs correspond to different model grid length scales (65, 125, 225 or 425 km).

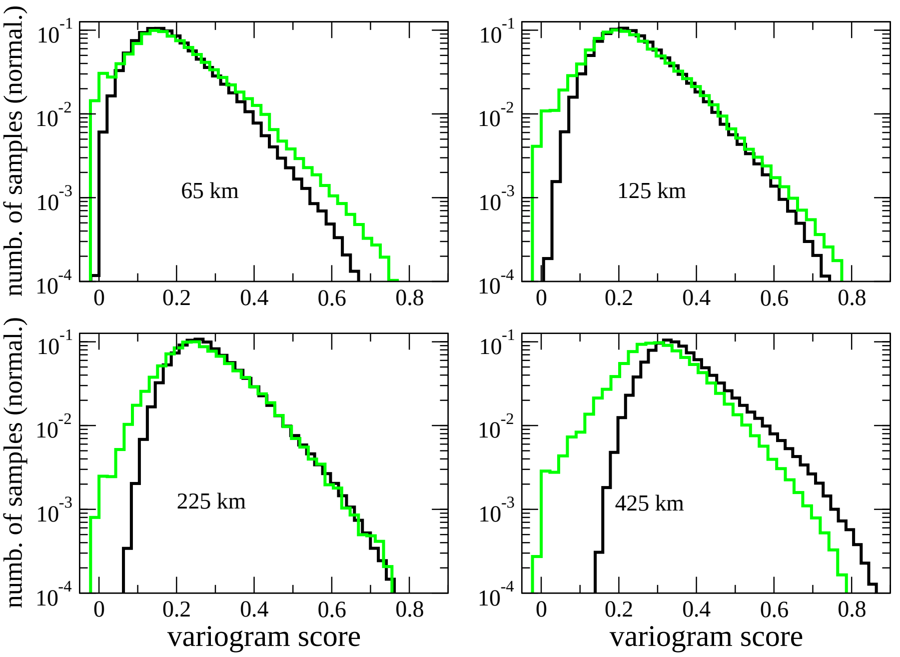

Figure 3.12: As Fig.3.11 but for the corresponding normalised number of samples.

the larger rain rate range ($rainrate > 10mm/h$) for which discrepancies are larger. For these comparably large rain rates, however, the number of samples is not very big which might partly influence these results.

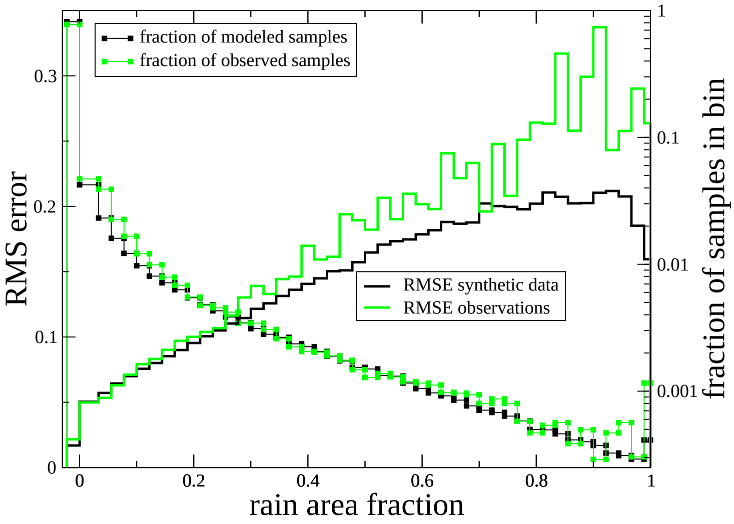

Figure 3.13: The same as Fig. 3.6 but RMS errors and number concentrations are computed for bins corresponding to rain-fraction intervals.

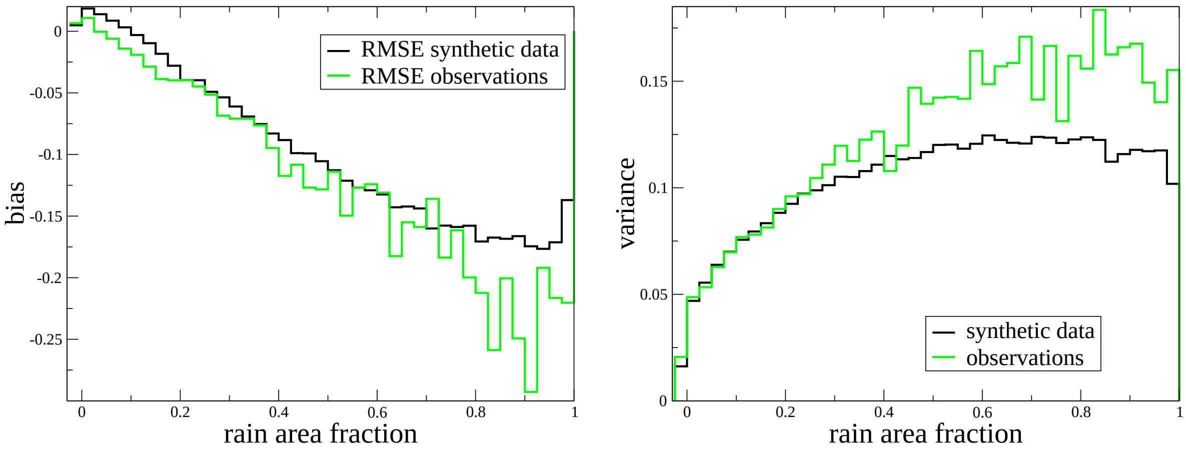

Figure 3.14: The same as Fig. 3.9 but for rain-fraction bins (instead of variogram-score bins).

Which measure is better?

Above we found that both types of measures, the variogram score as well as the measured variable itself (taking, e.g., the rain fraction for diagnosing the representativity error of the rain fraction data) seem to give useful measures for the flow dependency of the representativity error. This raises the question which of these scores is better? What we would like to have is a good discriminator which enables us to select as many as possible of the regions for which the error is small (so we can give them a high weight in the data assimilation process) and, also, to identify, as reliably as possible, those regions where the error is large.

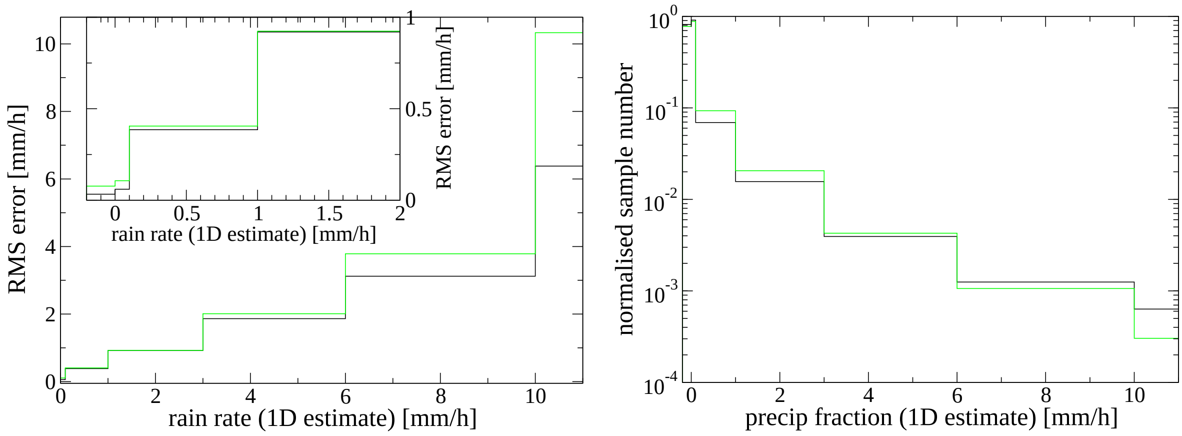

Figure 3.15: The same as Figure 3.13 but for rain rates (in rain-rate bins) instead of rain fraction.

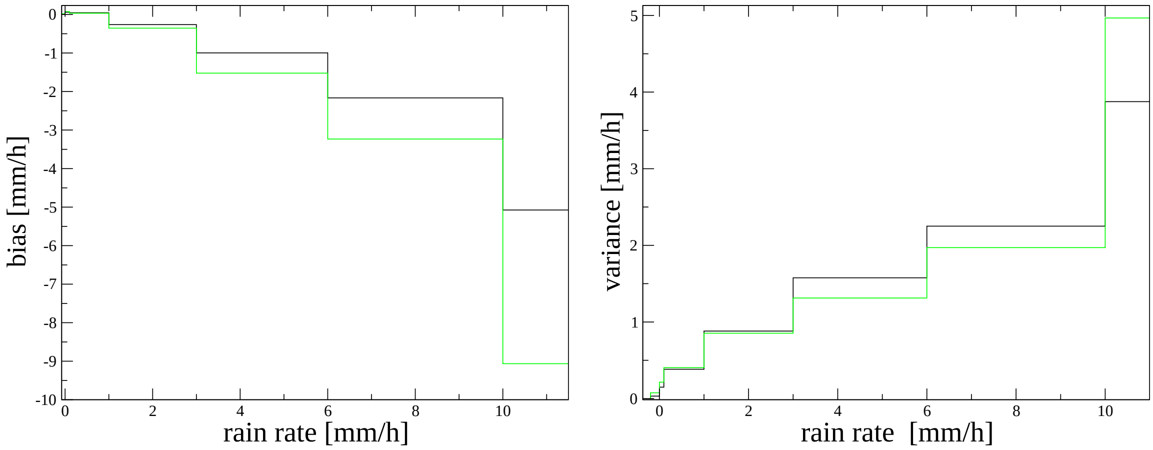

Figure 3.16: The same as Figure 3.14 but for rain rates (in rain-rate bins) instead of rain fraction.

The quality of a score therefore depends not only on how strongly the rms error varies with respect to the score, but also on how many of the data regions are located within the parameter regime where the score has good skill. To combine both of these aspects, we define the following variables:

$$\overline{rmse}_{av}\left(\tilde{sc}\right) = \int_{-\infty}^{\tilde{sc}} P_{dis}\left(\check{sc}\right) rmse\left(\check{sc}\right) d\check{sc} \tag{3.14}$$

$$\overline{nb}_{av}\left(\tilde{sc}\right) = \int_{-\infty}^{\tilde{sc}} P_{dis}\left(\check{sc}\right) d\check{sc}\,. \tag{3.15}$$

where $P_{dis}\left(\check{sc}\right)$ is the PDF for a chosen score $\check{sc}$ while $\overline{rmse}_{av}\left(\tilde{sc}\right)$ is the average root mean square error for all regions for which the obtained score is smaller or equal to $\tilde{sc}$. Equation 3.15 defines $\overline{nb}_{av}\left(\tilde{sc}\right)$ as the relative fraction of these regions.

Figure 3.17 shows $\overline{rmse}_{av}\left(\tilde{sc}\right)$ as a function of $\overline{nb}_{av}\left(\tilde{sc}\right)$ for different score functions (the corresponding values of $\tilde{sc}$ are not shown). This type of graph addresses the following question. If we use a certain score to select the, say, 80% grid boxes with the lowest error (i.e., if we select the 80% grid boxes which according to this score have the lowest error), how big is the average error within these 80% selected grid boxes. If the score was a perfect discriminator, this average error would be identical to the average error of the 80% grid boxes which truly have the smallest errors (and not just according to some score). This true average error has been included in Fig. 3.17 by the black curve. It gives a lower bound for the other curves.

Generally a score can be regarded as better than another score if its error in Fig. 3.17 is smaller for all sample fractions. In this respect, however, the result for the variogram score and rain-fraction score are mixed with the curves crossing each other (both curves are generally quite close together). The curve for the rain-fraction score (green curve), however, starts at much higher values of $\overline{nb}_{av}$ and $\overline{rmse}_{av}$ which is due to the fact that the bin with the smallest error (i.e., the bin where the precipitation fraction is zero) has a large number of points (almost 80%). The variogram score, however, can also differentiate between different subsets of the zero-precipitation-fraction bin and is able to identify regions where the representativity error is substantially smaller than the average value for this bin. The reason for this is that the variogram score uses information far beyond the grid box for which the precipitation fraction is being evaluated. This indicates that the variogram score is a better measure for the flow dependency of the representativity error.

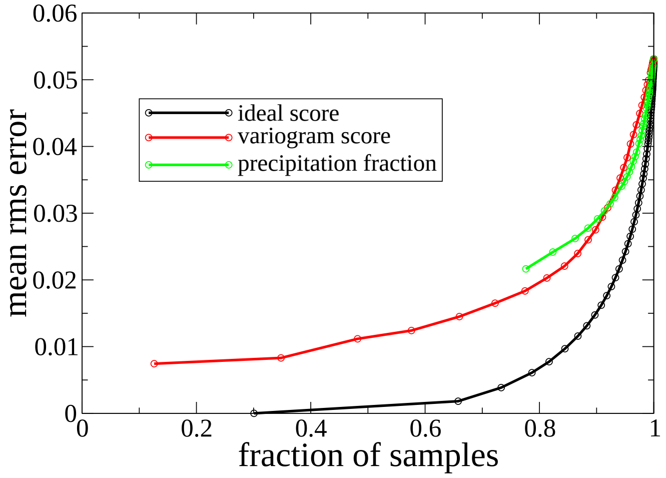

Figure 3.17: The average error $\overline{rmse}_{av}(\tilde{sc})$ (vertical axis; see Eq. 3.14) plotted against the corresponding fraction $\overline{nb}_{av}(\tilde{sc})$ (horizontal axis; see Eq. 3.15) for the observed TRMM rain fraction data. Colours red and green correspond to different score functions as indicated in the legend. The black curve (labelled "ideal score") gives a lower bound to the error which could be possibly achieved by a score (see text).

3.5 Summary and conclusions

A method to obtain a flow dependent estimate of the representativity error has been developed in this project. Tests with real world data indicate that the method gives useful estimates for data with very different statistical properties and can be used to determine biases and variances separately.

To our knowledge, this is the first method which computes estimates for these important quantities and which shows good potential for future operational use. While this is important for applications in data assimilation, the small footprint of the active satellite measurements appears in general to be a major obstacle for comparing them with atmospheric models. The extent to which the atmospheric modelling community can benefit from this new data type may therefore depend quite crucially on the further development of statistical up-scaling methods for which the work presented here is an example.

The method presented here is based on a quasi-empirical relationship between error characteristics and a measure ("score") of the variability along the satellite track. This relationship is obtained through stochastic modelling techniques for which standard methods have been generalised to cope with more general classes of data.

The score used in most of this work has been newly developed for this project and was named "variogram maximum score" (or short "variogram score") and is based on a probabilistic measure which is defined locally and which gives the decay of the covariance function along the satellite track. This variogram score was found to differentiate well between regions of small and large representativity error. It is more flexible than taking, e.g., cloud fraction (i.e., the measured variable itself) as an alternative score. With its capability to exploit information on different length scales along the satellite track, the variogram score can differentiate regions which have the same cloud fraction but for which the representativity error has different magnitudes.

While the work presented in this section demonstrates how the new method works for different types of data, applying it within the ECMWF data assimilation system will require some further, mainly technical, developments. The major part of this will be the statistical processing of the data from the active satellite measurements in order to obtain the PDFs and covariance functions required for the creation of synthetic data. The number of regions required will depend on how strongly the statistical properties of the cloud field (as measured by CALIPSO and CloudSat) change over the regions for which the case studies will be performed. A possible future operational implementation of the method would require a global coverage of the statistical cloud field properties.

The tests presented in subsection 3.4 also showed some limitations for the use of the synthetic data generated for this study. While the generated data proved very useful for estimating the representativity error (particularly in conjunction with the variogram score), their overall statistical distributions showed some clear differences to those of the observations. E.g. in Fig. 3.5, the distribution of MODIS data has a local peak for small variogram score values while the number of samples of the corresponding synthetic data decreases rapidly with decreasing variogram maximum score. One reason for this discrepancy is quite likely the insufficient representation of the covariance function for large distances (compare Figure 3.4c). Representing covariances on a large range of scales is, however, in general not a trivial task. It can be computational very expensive and, also, covariances measured over large distances are typically increasingly noisy. At least a partial solution to this problem could be achieved by the use of so called "conditional modelling techniques" (see Chiles and Delfiner, 1999, for an overview). The synthetic data generated by such techniques do not only share important statistical properties with the observations, they also coincide with the observations along the measurement tracks (stochastic modelling is only used to fill the gaps).

Another limitation of the stochastic modelling technique employed here is the use of a single Gaussian field to describe a cloud field which in general comprises different synoptic regimes. Methods which involve the combination of several Gaussian fields could lead to strong improvements. Such methods have been developed and employed for modelling indicator fields (e.g., for describing different geological facies, see Dowd *et al.*, 2003). The method developed within this project has great flexibility and can, in principle, be generalised to a multi-Gaussian approach (the central transformation 3.13 can be generalised in a straight forward way). While the corresponding (numerical) inversion of the covariance transformation becomes considerably more complex, such an approach seems very attractive as it could incorporate a more general type of flow dependence.

To summarise, the method developed has shown very promising capabilities for the estimation of the representativity errors involved with the small footprint of the new active satellite measurements. This was the main topic for this project. The generated synthetic data appear, however, less reliable for other applications which involve comparing more general statistical properties of NWP model data with the observations (such as PDFs or some aspects of these distributions, apart from the mean). Further developments and generalisations of the employed stochastic method are, however, very likely to improve these aspects considerably and may be very important for future uses of active satellite measurements in NWP. Such improvements would, of course, also further ameliorate the representativity error estimates discussed in this section of the report.

Acknowledgements

The NASA CloudSat Project is kindly acknowledged for providing the CloudSat data. The authors are also grateful to the Goddard Earth Sciences Data and Information Services Center (GES DISC) for providing TRMM PR and MODIS data.

A List of Acronyms

CALIPSO	Cloud-Aerosol Lidar and Infrared Pathfinder Satellite Observation
CFMIP	Cloud Feedback Model Intercomparison Project
CloudSat	NASA's cloud radar mission
COSP	CFMIP Observation Simulator Package
CPR	Cloud Profiling Radar
CPU	Central Processing Unit
ECMWF	European Centre for Medium Range Weather Forecasts
ESA	European Space Agency
GCM	General (or Global) Circulation Model
GES DISC	Goddard Earth Sciences Data and Information Services Center
HC	Hydrometeor Content
IFS	Integrated Forecasting System
ISCCP	International Satellite Cloud Climatology Project
MC	Multi-Column
MODIS	Moderate Resolution Imaging Spectroradiometer
NASA	National Aeronautics and Space Administration
NWP	Numerical Weather Prediction
PDF	Probability density function
PSD	Particle Size Distribution
RMS	root mean square error
SC	Single-Column
SCOPS	Subgrid Cloud Overlap Profile Sampler
TRMM	Tropical Rainfall Measuring Mission
ZmVar	Z (reflectivity) Model for Variational assimilation of ECMWF

References

Bauer, P., A. Khain, A. Pokrovsky, R. Meneghini, C. Kummerow, F. Marzano, and J. P. V. P. Baptista, 2000: Combined cloud–microwave radiative transfer modeling of stratiform rainfall, *J. Atmos. Sci.*, **57**(8), 1082–1104.

Benedetti, A. and M. Janisková, 2004: Advances in cloud assimilation at ECMWF using ARM radar data, *Extended abstract for ICCP, Bologna*.

Benedetti, A., P. Lopez, E. Moreau, P. Bauer, and V. Venugopal, 2005: Verification of TMI-adjusted rainfall analyses of tropical cyclones at ECMWF using TRMM precipitation radar, *Journal of Applied Meteorology*, **44**(11), 1677–1690.

Bodas-Salcedo, A., M. J. Webb, M. E. Brooks, M. A. Ringer, K. D. Williams, S. F. Milton, and D. R. Wilson, 2008: Evaluating cloud systems in the Met Office global forecast model using simulated CloudSat radar reflectivities, *J. Geophys. Res.-Atmospheres*, **113**(D00A13).

Brown, P. R. A. and P. N. Francis, 1995: Improved measurements of the ice water content in cirrus using a total-water probe, *Journal of Atmospheric and Oceanic Technology*, **12**(2).

Bruggeman, D. A. G., 1935: Calculation of different physical constants of heterogeneous substances, *Ann Phys*, **24**, 636–679.

Chiles, J. and P. Delfiner, 1999: *Geostatistics: modeling spatial uncertainty*, Wiley-Interscience.

Chiriaco, M., R. Vautard, H. Chepfer, M. Haeffelin, J. Dudhia, Y. Wanherdrick, Y. Morille, and A. Protat, 2006: The ability of MM5 to simulate ice clouds: Systematic comparison between simulated and measured fluxes and lidar/radar profiles at the SIRTA atmospheric observatory, *Mon. Wea. Rev.*, **134**(3), 897–918.

Clothiaux, E. E., M. A. Miller, B. A. Albrecht, T. P. Ackerman, J. Verlinde, D. M. Babb, R. M. Peters, and W. J. Syrett, 1995: An evaluation of a 94-GHz radar for remote sensing of cloud properties, *J. Ocean. Atmos. Tech.*, **12**(2), 201–229.

Deirmendjian, D., 1969: Light scattering on spherical polydispersions.

Dowd, P., E. Pardo-Igúzquiza, and C. Xu, 2003: Plurigau: a computer program for simulating spatial facies using the truncated plurigaussian method, *Computers and Geosciences*, **29**(2), 123–141.

Haynes, J. M., T. S. L'Ecuyer, G. L. Stephens, S. D. Miller, C. Mitrescu, N. B. Wood, and S. Tanelli, 2009: Rainfall retrieval over the ocean with spaceborne W-band radar, *J. Geophys. Res.-Atmospheres*, **114**(null).

Haynes, J. M., R. T. Marchand, Z. Luo, A. Bodas-Salcedo, and G. L. Stephens, 2007: A multipurpose radar simulation package: QuickBeam, *Bull. Am. Meteorol. Soc.*, **88**(11), 1723–1727.

Hong, G., P. Yang, B. A. Baum, and A. J. Heymsfield, 2008: Relationship between ice water content and equivalent radar reflectivity for clouds consisting of nonspherical ice particles, *J. Geophys. Res.-Atmospheres*, **113**(D20), D20205.

Janisková, M., 2004: Impact of EarthCARE products on Numerical Weather Prediction, *Contract report to the European Space Agency, 59 pp*.

Kollias, P. and B. Albrecht, 2005: Why the melting layer radar reflectivity is not bright at 94 GHz, *Geophys. Res. Lett*, **32**.

Liebe, H. J., 1985: An updated model for millimeter wave propagation in moist air, *Radio Science*, **20**(5), 1069–1089.

Liebe, H. J., G. A. Hufford, and T. Manabe, 1991: A model for the complex permittivity of water at frequencies below 1 THz, *International Journal of Infrared and Millimeter Waves*, **12**(7), 659–675.

Liebe, H. J., P. W. Rosenkranz, and G. A. Hufford, 1992: Atmospheric 60-GHz oxygen spectrum- New laboratory measurements and line parameters, *Journal of Quantitative Spectroscopy and Radiative Transfer*, **48**(5), 629–643.

Liu, G., 2004: Approximation of single scattering properties of ice and snow particles for high microwave frequencies, *J. Atmos. Sci.*, **61**(20), 2441–2456.

Lopez, P., A. Benedetti, P. Bauer, M. Janisková, and M. Köhler, 2006: Experimental 2D-Var assimilation of ARM cloud and precipitation observations, *Qurt. J. Roy. Meteor. Soc.*, **132**, 1325–1347.

Mätzler, C. and U. Wegmüller, 1988: Dielectric properties of fresh-water ice at microwave frequencies, *Journal of Physics D: Applied Physics*, **21**, 1660.

Maxwell Garnett, J. C., 1904: Colours in metal glasses and metal films, *Trans. R. Soc. London*, **203**, 385–420.

Miller, S., R. Bankert, J. Forsythe, C. Mitrescu, D. Reinke, and R. Austin, 2007: Expanding Curtain Observations of Cloud Vertical Structure and Layering to Model-Relevant Spatial Scales, in *American Geophysical Union, Fall Meeting 2007, abstract# A53D-1438*.

Pardo-Iguzquiza, E. and M. Chica-Olmo, 1993: The Fourier integral method: an efficient spectral method for simulation of random fields, *Mathematical Geology*, **25**(2), 177–217.

Pardo-Igúzquiza, E. and M. Chica-Olmo, 1994: SPECSIM: a program for simulating random fields by an improved spectral approach, *Computers & Geosciences*, **20**(4), 597–613.

Raisanen, P., H. W. Barker, M. F. Khairoutdinov, J. Li, and D. A. Randall, 2004: Stochastic generation of subgrid-scale cloudy columns for large-scale models, *Qurt. J. Roy. Meteor. Soc.*, **130**(601).

Ray, P. S., 1972: Broadband complex refractive indices of ice and water, *Applied Optics*, **11**(8), 1836–1844.

Ryan, B. F., 2000: A bulk parameterization of the ice particle size distribution and the optical properties in ice clouds, *J. Atmos. Sci.*, **57**(9), 1436–1451.

Tian, L. and J. A. Curry, 1989: Cloud overlap statistics, *J. Geophys. Res.-Atmospheres*, **94**(D7).

Warren, S. G., 1984: Optical constants of ice from the ultraviolet to the microwave, *Applied Optics*, **23**(8), 1206–1225.

Warren, S. G. and R. E. Brandt, 2008: Optical constants of ice from the ultraviolet to the microwave: A revised compilation, *J. Geophys. Res*, **113**(D14).

Webb, M., C. Senior, S. Bony, and J.-J. Morcrette, 2001: Combining ERBE and ISCCP data to assess clouds in the Hadley Centre, ECMWF and LMD atmospheric climate models, *Climate Dynamics*, **17**(12), 905–922.